

Long-Range Population Dynamics of Anatomically Defined Neocortical Networks

Jerry L. Chen^{1,*†}, Fabian F. Voigt^{1,2,*}, Mitra Javadzadeh¹, Roland Krueppel^{1,‡}, and Fritjof Helmchen^{1,2}

¹Brain Research Institute, University of Zurich, Switzerland. ²Neuroscience Center Zurich, University of Zurich and ETH Zurich, Zurich, Switzerland

**equal contribution*

[†]Present address: Department of Biology, Boston University, Boston, MA, USA, 02215

[‡]Present address: Federal Ministry of Education and Research, Bonn, Germany, 53175

Summary

The coordination of activity across neocortical areas is essential for mammalian brain function. Understanding this process requires simultaneous functional measurements across the cortex. In order to dissociate direct cortico-cortical interactions from other sources of neuronal correlations, it is furthermore desirable to target cross-areal recordings to neuronal subpopulations that anatomically project between areas. Here, we combined anatomical tracers with a novel multi-area two-photon microscope to perform simultaneous calcium imaging across mouse primary (S1) and secondary (S2) somatosensory whisker cortex during texture discrimination behavior, specifically identifying feedforward and feedback neurons. We find that coordination of S1-S2 activity increases during motor behaviors such as goal-directed whisking and licking. This effect was not specific to identified feedforward and feedback neurons. However, these mutually projecting neurons especially participated in inter-areal coordination when motor behavior was paired with whisker-texture touches, suggesting that direct S1-S2 interactions are sensory-dependent.

Our results demonstrate specific functional coordination of anatomically-identified projection neurons across sensory cortices.

Main Text

INTRODUCTION

Sensory perception, fine voluntary motor control, and higher cognitive functions depend on neural dynamics in the mammalian neocortex, which itself relies on the exchange of information between cortical areas through both bottom-up (feedforward) and top-down (feedback) neuronal pathways across the cortical hierarchy (Bressler and Menon, 2010; Buschman and Miller, 2007). Cortico-cortical connections are formed between columnar microcircuits via long-range axons of pyramidal neurons in superficial layer 2/3 (L2/3) and deeper layer 5. A given cortical area typically establishes connectivity patterns not only with one particular area but with multiple target areas in a distributed and often reciprocal fashion (Markov et al., 2013; Oh et al., 2014; Zingg et al., 2014). Thus, in order to fully understand the cortical interactions underlying behavior, it is necessary to disentangle how neuronal subpopulations defined by both their functional properties and their specific anatomical projections contribute to local computation and long-range communication.

Such an understanding has been limited by the difficulty in measuring population activity across areas with sufficient spatial and temporal resolution. Present methods to study large-scale cortical dynamics either lack cellular resolution and sensitivity to low numbers of action potentials (e.g., human fMRI; Hutchison et al., 2013) or wide-field functional imaging in mice (Ferezou et al., 2007; Lim et al., 2013; Minderer et al., 2012) or they are restricted to poorly defined neuronal subsets as for extracellular recordings (Melzer et al., 2006). The main

limitation for these recording approaches is the reliance on correlated activity patterns to infer information flow without the additional ability to attribute such activity to anatomically-defined neuronal subsets. Consequently, it has not been possible to definitively determine whether the underlying measured inter-areal dynamics could reflect: i) direct cortico-cortical interactions; ii) indirect cortico-thalamocortical pathways; iii) or synaptic drive from common input areas. To dissect these possibilities new technologies are needed to monitor inter-areal dynamics with cellular resolution while at the same time identifying subsets of neurons that project across areas. Two-photon microscopy is well suited to monitor action potential firing across neuronal populations, mainly using calcium imaging, as well as to optically identify molecularly or anatomically-defined cell types (Chen et al., 2013a). So far, standard two-photon microscopes have been limited to imaging long-range activity within one cortical area (Chen et al., 2013b; Glickfeld et al., 2013; Jarosiewicz et al., 2012; Petreanu et al., 2012; Sato and Svoboda, 2010). New systems have recently been developed that enable simultaneous imaging of neuronal populations across cortical areas across increasingly larger fields of view (Lecoq et al., 2014; Stirman et al., 2014; Tsai et al., 2015).

Here, we present a novel “multi-area” two-photon microscope for simultaneous measurements across primary and higher sensory areas of mouse neocortex. We have combined this system with anatomical labeling strategies to identify feedforward and feedback projection neurons between reciprocally connected cortical areas to image their functional interactions. In order to investigate the role of direct cortico-cortical interactions among other potential sources of correlated activity, we have applied this approach in the whisker primary (S1) and secondary (S2) somatosensory cortices, two areas that are anatomically coupled through reciprocal connections, cortico-thalamocortical pathways, and other common inputs (Deschenes et al., 1998; Suter and Shepherd, 2015; Theyel et al., 2010). Expanding our recent work on the activity of

divergent projection pathways originating in S1 during a texture discrimination task (Chen et al., 2013b; Chen et al., 2015), we sought here to examine how population activity in S1 and S2 evolves over time during such tactile whisker-based behavior. Whisking behavior spans a range of time scales, from individual whisk cycles of about 100-ms duration, to bouts of whisking over a second, and to prolonged whisking, for example during locomotion (Kleinfeld and Deschenes, 2011). Our multi-area imaging approach enabled us to analyze the slower aspects of whisking envelope changes and whisker-touch contacts whereas analysis of neuronal dynamics on the rapid time scale of tens of milliseconds was precluded by our limited temporal resolution. Our main goal was, however, to take advantage of the ability to simultaneously image in S1 and S2 and to investigate how the subsets of reciprocally projecting neurons contribute to the coordination of activity across these areas and to the coding of sensory and behavior information.

RESULTS

Multi-area two-photon microscope

We built a two-photon microscope capable of simultaneous scanning of two sub-areas within a relatively large field of view (FOV), enabling one to freely and independently position the sub-areas in order to select appropriate imaging spots. To achieve this goal we coupled two laser beams through a galvanometric scanner system into a low-magnification, high-NA objective (**Figure 1A-D and Materials and Methods**). Specifically, we chose a 16x water-immersion Nikon objective (NA 0.8) as core element, which supports imaging in a FOV of 1.8-mm maximum side length with cellular resolution (**Figure 1E, Figure 1–figure supplement 1 and Video 1**). We split laser light from a Ti:sapphire laser (80 MHz pulse repetition rate) into two excitation beams using a 50:50 beam splitter and delayed the laser pulse train of one beam by 6.25 ns, half of the inter-pulse interval, to interlace the two pulse trains so that the two sub-areas

99 receive alternating laser excitation pulses. For disambiguating the fluorescence signal generated
100 by the two laser foci, we adopted a rapid de-multiplexing approach (Cheng et al., 2011). For
101 typical 2-4 ns fluorescence lifetimes of fluorescent proteins (Akerboom et al., 2013), the 6.25-ns
102 time windows are sufficiently long to capture mainly fluorescence photons generated by the last
103 excitation pulse. Some crosstalk between areas may remain but can be corrected for post hoc
104 using spatial linear unmixing (**Materials and Methods and Figure 1–figure supplement 2**)
105 (Cheng et al., 2011).

106 Each beam enters a movable coupling unit, named 'focal plane unit' (FPU), which enables
107 independent positioning and focusing of its respective imaging area below the objective (**Figure**
108 **1A-C**). Independent positioning is achieved by coupling the FPU output beams to the scanner
109 unit via small fold mirrors that sit at the end of cantilever arms. Lateral X/Y-movement of each
110 FPU introduces an offset of the respective beam from the optical axis of the first scan lens, which
111 converts this offset into a pivoting angle of the beam around the scan mirrors. In the remaining
112 optical path, this pivoting angle is translated into lateral movement of the corresponding imaging
113 sub-area below the objective. Independent focusing is achieved with electrically tunable lenses
114 (ETLs) in the FPUs (Grewe et al., 2011). Each ETL is combined with an offset lens to allow
115 tuning the beam from divergent to convergent. These divergence changes translate into axial
116 shifts of the intermediate foci at the FPU output and in between scan and tube lens, corresponding
117 to down- and upward shifts of the excitation focus along the optical Z-axis below the objective.
118 In combination with a 6-mm pair of scan mirrors, ETL focusing provides a Z-range of up to 600
119 μm .

120
121 **Imaging anatomically-identified projection neurons across S1 and S2**

Mice can actively sense the environment by moving their whiskers to gather information regarding the location, shape, size, and texture of an object (Diamond et al., 2008). Processing of tactile information at the cortical level is thought to occur through interactions between S1, S2, as well as primary motor cortex (M1) (Aronoff et al., 2010; Bosman et al., 2011). In order to investigate direct interactions between S1 and S2, we sought to apply the multi-area two-photon microscope to simultaneously monitor activity in feedforward neurons in S1 projecting to S2 ($S1_{S2}$) and feedback neurons in S2 projecting to S1 ($S2_{S1}$) in wild-type adult mice during tactile whisker behavior. To distinctly label these projection neurons in a mutually exclusive manner across the reciprocally connected areas we employed a viral strategy making use of orthogonal recombinase systems. To label $S2_{S1}$ neurons, we delivered a retrogradely-infecting AAV6 expressing Cre recombinase (AAV6-*pgk-Cre*) into S1 along with S2-injection of an AAV1 expressing Cre-dependent nuclear tdTomato (AAV1-*EF1 α -dio-NLStdTomato*; **Figure 2A**). $S1_{S2}$ neurons were labeled by delivering an AAV6 expressing Flpe (AAV6-*syn-Flpe*) into S2 along with S1-injection of an AAV1 expressing Flpe-dependent nuclear LSSmKate2 (AAV1-*EF1 α -fio-H2BLSSmKate2*). In addition to these viruses, we broadly expressed the genetically encoded calcium indicator YC-Nano140 in S1 and S2 using AAV1-*EF1 α -YCNano140* (Chen et al., 2013b; Horikawa et al., 2010). For targeting viral injections as well as for selecting regions for later two-photon imaging, we employed optical intrinsic signal imaging to identify areas within S1 and S2 corresponding to the same principal whisker (**Figure 2B and Materials and Methods**).

Following cranial window implantation, LSSmKate2-positive $S1_{S2}$ neurons and tdTomato-positive $S2_{S1}$ neurons in L2/3 were identified *in vivo* (**Figure 2C**). YC-Nano140 expressing neurons that did not express LSSmKate2 or tdTomato were classified as $S1_{ND}$ and $S2_{ND}$ neurons, respectively (target area 'not determined'), possibly comprising unlabeled $S1_{S2}$ and

S2_{SI} neurons as well as projection neurons targeting different brain regions. Animals were habituated to head-fixation and trained to perform a whisker-based go/no-go texture discrimination task (**Figure 2D,E**) (Chen et al., 2013b; Chen et al., 2015). On ‘go’ trials, animals were rewarded with a water droplet if they correctly licked (‘Hit’) when presented with a target texture (a panel of coarse sandpaper, P100). On ‘no-go’ trials, mice were supposed to withhold licking (‘correct rejection’ or ‘CR’) when presented with one of two non-rewarded, ‘non-target’ textures of smoother grades (P280, P1200). Misses on go trials were not rewarded and false alarms (‘FA’) on no-go trials were punished with an air puff and a time-out period. Whisker movements were monitored with high-speed videography (500 Hz) and licking behavior was measured with a piezo film attached to the water spout. Whisking and licking recordings were downsampled to match the frame rate of imaging (7 Hz), allowing analysis of how neuronal activity relates to slow amplitude changes of whisking envelope and to the occurrence of whisker-texture touches (**Materials and Methods**).

Since simultaneous imaging in two cortical regions presents unique opportunities to examine the coordination of activity across areas, we sought to increase the number of pairwise imaged S1 and S2 neuronal populations. To this end we used the ETLs to implement a ‘combinatorial plane hopping’ mode, in which two sub-areas are scanned simultaneously but each imaging plane is independently refocused in a combinatorial manner during the inter-trial interval (**Figure 2C,F and Video 2**). Using this approach, we imaged in 7 mice ~150 neurons per sub-area (distributed over three imaging planes at different cortical depths) across ~1800 trials over 5-6 experimental sessions. Combinatorial hopping between three imaging planes in each area resulted in simultaneous imaging of 9 combinations of planes per animal, for which ~200 trials were acquired per pair of planes, still sufficient for our analysis. In total, 228 S1_{S2}, 817 S1_{ND}, 193 S2_{SI}, and 750 S2_{ND} neurons were imaged in 63 pairs of focal planes across S1 and

S2. For comparison with non-task conditions, we additionally imaged the same neuronal populations as measured during texture discrimination behavior for another ~1800 trials over 5-6 sessions, during which mice were passively presented with the same textures. In order to improve statistical analysis of single-trial responses for trial conditions with low trial numbers, calcium traces were denoised using tensor decomposition (**Figure 2-figure supplement 1 and source data file 1, Materials and Methods**).

Behavior-related responses of S1 and S2 neurons

While sensory- and behavior-related responses of S1_{S2}, S1_{M1}, and S1_{ND} neurons have been characterized during texture discrimination (Chen et al., 2013b; Chen et al., 2015), responses of S2_{S1} and S2_{ND} neurons have not. We first assessed for each cell class how calcium signals relate to behavioral aspects using a general linear model (GLM) against vectors for whisker-touch onset, whisking envelope amplitude, and licking onset (**Figure 3A,B and Figure 3-figure supplement 1**) (Miri et al., 2011; Pinto and Dan, 2015). S1_{ND} and S2_{S1} neurons showed better overall GLM fits to these behavioral parameters compared to their neuronal counterparts in their respective areas (**Figure 3C and Figure 3-figure supplement 1**; S1_{ND} vs. S1_{S2}, $P < 0.002$; S2_{ND} vs. S2_{S1}, $P < 0.005$, KS-test). Further analysis of fits to specific regressors revealed that S2_{S1} and S1_{ND} neurons showed higher GLM coefficients for whisker-touch onset than their within-area counterparts (**Figure 3D**; S1_{ND} vs. S1_{S2}, $P < 0.05$; S2_{ND} vs. S2_{S1}, $P < 0.005$, one-way ANOVA with repeated measures). While no specific differences were observed for cell classes in S1, S2_{S1} neurons showed higher GLM coefficients than S2_{ND} neurons for whisking and licking onset ($P < 0.001$, one-way ANOVA with repeated measures). These results suggest that S2_{S1} neurons exhibit higher whisking- and licking-related activity compared to other neurons in S2.

We next analyzed single-neuron responses to different sensory conditions or different behavior conditions by performing single-cell receiver operating characteristic (ROC) analysis against different trial conditions (Green and Swets, 1966). Single-cell ROC analysis of Hit vs. CR trials revealed that a larger fraction of S2_{S1} neurons compared to other neuronal classes (72%) was able to discriminate these two conditions above chance (**Figure 3E**; $P < 0.002$, χ^2 test). Differences between Hit vs. CR trials could reflect encoding of sensory information, decision, or decision-related actions such as licking. To disambiguate these possibilities, we also performed ROC analysis of FA vs. CR trials, which were previously shown to consist of similar whisking and sensory conditions (Chen et al., 2015). Again, a larger fraction of S2_{S1} neurons (50%) was able to discriminate these two conditions above chance ($P < 0.05$, χ^2 test), suggesting that this greater discrimination power of S2_{S1} neurons represents decision- or action-related information. As an additional control, we assessed sensory-related responses by ROC analysis of P280 vs. P1200 textures on CR trials and found that S2_{S1} neurons were not more likely to discriminate these trial types compared to other cell types (**Figure 3E**). Overall, we find that S2_{S1} were more likely to encode for non-sensory aspects of task-related behavior compared to other neurons in S2 and S1.

Motor-related coordination of S1 and S2

In order for task-related information exchange to occur between areas, activity across areas must be “coordinated” during relevant behavioral conditions and such coordination should be specific to neurons that anatomically project between areas. To investigate how activity is coordinated across S1 and S2, we first sought a measure of population activity for each area that would capture the diverse response properties of individual neurons and allow us to determine if their dynamics evolve similarly across time. To this end, we characterized population activity in S1

and S2, respectively, by using linear discriminant analysis (LDA) (Fisher, 1936; Safaai et al., 2013). For n neurons in an imaging area, LDA finds for each time point an axis in n -dimensional space so that the distributions of population responses for two chosen trial conditions – projected onto this axis – are best separated (**Materials and Methods**). Similar to the ROC analysis, we selected not only Hit vs. CR but also various other pairs of trial conditions that would allow us to disambiguate sensory- and behavior-related dynamics (**Table 1**). The dimensionality reduction resulting from this approach effectively extracts time-dependent ‘linear discriminant’ variables $LD(t)$ as one-dimensional representations of neuronal population activity with respect to the chosen trial conditions. For illustration purposes, we exemplify this LDA procedure for measurements from only two neurons in **Figure 4A,B**, whereas typically populations of active neurons within an imaging area were used for analysis.

In the initial analysis of population responses, we did not distinguish between neuronal cell types in each area and thus included both $S1_{S2}$ and $S1_{ND}$ neurons for S1 and $S2_{S1}$ and $S2_{ND}$ neurons for S2. We performed LDA at each time point for 1-s periods prior to and following either whisker-touch onset or licking onset, generating mean LD time courses for S1 or S2 by averaging LDA results from all imaging areas in these respective regions. For LDA performed on Hit vs. CR trials, we observed that mean population responses for both S1 and S2 diverged following whisker-touch onset (**Figure 4C**). ROC analysis using the LD variable as measure of population activity in S1 and S2, respectively, revealed that discrimination power for both areas increased immediately following whisker-touch onset and through the first second of touch (**Figure 4D**).

S1 and S2 receive common input from several areas including M1, which controls licking and whisking (Brecht et al., 2004; Huber et al., 2012; Suter and Shepherd, 2015), the posteromedial thalamic nucleus (POm), which relays re-afferent whisking (Deschenes et al.,

1998; Moore et al., 2015; Yu et al., 2006), and the ventral lateral region of the ventral posterior medial thalamic nucleus (VPMvl), which relays whisker touch (Pierret et al., 2000). Correlations of activity between S1 and S2 could thus reflect these aspects of behavior. To measure how S1 and S2 activities are coordinated across time, we calculated the trial-by-trial correlation of LD_{S1} and LD_{S2} , the LD time courses obtained for active neurons in simultaneously imaged populations in S1 and S2, respectively (**Figure 5A**). We termed this cross-areal correlation $LDCC_{S1:S2}$, which during task performance increased immediately following whisker-touch onset for both Hit and CR trials. 500 ms after touch onset, however, $LDCC_{S1:S2}$ remained elevated for Hit trials relative to CR trials (**Figure 5B**, $P < 0.05$, one-way ANOVA with repeated measures). The time point of this divergence corresponded to the average delay of licking onset from whisker-touch onset (mean reaction time: 524 ± 5 ms for Hit trials; **Figure 5C**) (Chen et al., 2013b; Chen et al., 2015). To examine whether $LDCC_{S1:S2}$ changes indeed relate to the reaction time, $LDCC_{S1:S2}$ on Hit trials were re-aligned to licking onset (**Figure 5D**). $LDCC_{S1:S2}$ increased and peaked at licking onset and remained elevated thereafter, further suggesting that coordination of activity across S1 and S2 could be associated with such behavior.

To dissociate whether and how cross-areal coordination related to sensory versus motor parameters, we first controlled for sensory input by measuring $LDCC_{S1:S2}$ for population responses projected along the FA vs. CR axis, where the same non-target textures were presented (**Figure 5E and Figure 5-figure supplement 1A,B**). We found $LDCC_{S1:S2}$ was higher for FA compared to CR trials both prior to and following whisker-touch onset, ($P < 0.05$, one-way ANOVA with repeated measures). We asked if this increased $LDCC_{S1:S2}$ on FA trials could partially be explained by licking behavior. We therefore subdivided FA trials into trials in which licking preceded whisker-touch onset – likely reflecting impulsive licking behavior – and those trials in which licking onset occurred after whisker-touch onset (67.1% and 32.9% of FA trials,

respectively; **Figure 5F**). $LDCC_{S1:S2}$ showed an increased level prior to whisker-touch onset specifically for the subset of trials with early licking (**Figure 5G**, $P<0.05$, one-way ANOVA with repeated measures). This suggests that population activity in S1 and S2 can be coordinated during licking behavior both in the presence and absence of sensory stimulation.

We next asked whether $LDCC_{S1:S2}$ is also related to other motor behaviors such as whisking. During texture discrimination, animals adopted a high-amplitude, rhythmic whisking strategy prior to whisker-touch onset in anticipation of the delivered texture, which drives texture-specific kinematics and is absent in non-task sessions (Chen et al., 2013b; Chen et al., 2015). During task conditions, we measured $LDCC_{S1:S2}$ from population responses for CR trials (i.e. same texture, no licking) projected along the high- vs. low-amplitude whisking axis (**Figure 5H and Figure 5-figure supplement 1C-D**). Similar to the results for licking behavior, high-amplitude whisking trials were associated with higher $LDCC_{S1:S2}$ prior to and after whisker-touch onset when compared to low-amplitude whisking trials (**Figure 5I**, $P<0.02$, one-way ANOVA with repeated measures), demonstrating another motor-related component of S1-S2 coordination. By using LDA for other pairs of trial conditions, we found that stimulation with distinct textures did not result in elevated $LDCC_{S1:S2}$, suggesting that S1-S2 coordination is not stimulus-specific (**Figure 5-figure supplement 1G-H and Figure 5-figure supplement 2**). Taken together, this demonstrates that the coordination of population activity across S1 and S2 can be associated with licking and whisking behavior that is independent of sensory stimulus.

Projection neurons contribute to coordinated activity

Correlated changes in population dynamics across cortical areas can either reflect direct cortico-cortical interactions, indirect interactions through cortico-thalamocortical pathways, or co-activation from another common input source (Salinas and Sejnowski, 2001). In order for direct

cortico-cortical interactions to be present, such correlations should exist in neurons that project between those areas. To understand how $S1_{S2}$ and $S2_{S1}$ neurons might contribute to the coordination of population activity in S1 and S2, we repeated the LDA for S1 or S2 but shuffled the trial-by-trial responses of $S1_{S2}$ and $S2_{S1}$ neurons when projecting the population response onto the LD axis (**Figure 6-figure supplement 1A**). In order to ensure that changes in the population response were specific to these neurons and not merely a result of altering any given subpopulation of neurons, we also computed population responses, in which trials from an equal number of $S1_{ND}$ and $S2_{ND}$ neurons were shuffled (see details in **Materials and Methods**). We observed no significant difference in the trajectory or discrimination power of S1 and S2 population responses when shuffling any of these cell types (**Figure 6-figure supplement 2**), suggesting that the average population response within each area was not altered with this analysis.

To determine the specific contribution of $S1_{S2}$ and $S2_{S1}$ to inter-areal coordination, we measured the change in correlation between the S1 and S2 population responses ($\Delta LDCC_{S1:S2}$; relative to unshuffled controls) that resulted from shuffling trials of these projection neurons and compared it to the result of shuffling trials of $S1_{ND}$ and $S2_{ND}$ neurons (**Figure 6A and Figure 6-figure supplement 1B**). If $S2_{S1}$ and $S1_{S2}$ neurons especially contribute to $LDCC_{S1:S2}$, their trial-shuffling should lead to a larger reduction (more negative $\Delta LDCC_{S1:S2}$) compared to trial-shuffling $S1_{ND}$ and $S2_{ND}$ neurons. Analysis of coordinated activity projected along the Hit vs. CR axis showed no significant difference in $\Delta LDCC_{S1:S2}$ between $S2_{S1}$ and $S1_{S2}$ neurons and $S2_{ND}$ and $S1_{ND}$ neurons when aligned to whisker-touch onset (**Figure 6-figure supplement 3**). However, analysis of Hit trials after aligning to licking onset revealed a negative dip in $\Delta LDCC_{S1:S2}$ when shuffling projection neurons, indicating that $S1_{S2}$ and $S2_{S1}$ neurons especially

contributed to $LDCC_{S1:S2}$ upon licking onset (**Figure 6B**, $P<0.0001$, one-way ANOVA with repeated measures).

We further assessed the contribution of $S2_{S1}$ and $S1_{S2}$ neurons to inter-areal coordination along motor conditions by analyzing whisking- and licking-related $LDCC_{S1:S2}$. We first measured $\Delta LDCC_{S1:S2}$ from population responses projected onto the high- vs. low-whisking amplitude axis (for CR trials) and found that $S1_{S2}$ and $S2_{S1}$ neurons significantly contributed to $LDCC_{S1:S2}$ in high-amplitude whisking trials following but not preceding whisker-touch onset (**Figure 6C**, $P<0.02$, one-way ANOVA with repeated measures). Similarly, analysis of FA vs. CR trials showed that $S2_{S1}$ and $S1_{S2}$ neurons did not specially contribute to $LDCC_{S1:S2}$ for FA trials, in which licking onset preceded whisker-touch onset (**Figure 6D**), but they did so for trials, in which licking onset followed whisker-touch onset (**Figure 6E**, $P<0.02$, one-way ANOVA with repeated measures). These findings indicate that while licking and whisking behavior is associated with correlations in population responses across S1 and S2, any special contribution of $S1_{S2}$ and $S2_{S1}$ neurons to this coordination depends on the presence of the specific sensory stimulus, thus occurring after the whisker-touch onset. Hence, the specific contribution of projection neurons mutually connecting S1 and S2 could reflect sensory- rather than motor-related activity. In line with this notion, further analysis showed that $\Delta LDCC_{S1:S2}$ decreased when trial-shuffling $S1_{S2}$ and $S2_{S1}$ neurons compared to $S1_{ND}$ and $S2_{ND}$ neurons following whisker-touch onset on CR trials, when licking behavior is absent (**Figure 6F**, $P<0.02$, one-way ANOVA with repeated measures). These results demonstrate that direct cortico-cortical interactions through $S1_{S2}$ and $S2_{S1}$ neurons reflect exchange of sensory or decision information rather than motor information.

Discussion

In summary, we have demonstrated simultaneous measurement of calcium signals in identified feedforward and feedback neurons across S1 and S2 in the awake behaving mouse using a multi-area two-photon microscope in combination with viral-mediated labeling of long-range projection neurons. We have used this approach to investigate the contribution of cortico-cortical projection neurons to the coordinated activity patterns across these areas. While the acquisition rate of the imaging system and the kinetics of the expressed calcium indicator (Chen et al., 2013b) used in this study precludes our ability to capture the 4-10 ms spike latencies reported across mouse cortical areas (Ferezou et al., 2007) for examining spike-timing and monosynaptic relationship of long-range cortical dynamics, we nevertheless observe that population activity across S1 and S2 is coordinated during relevant task periods in a behavior-dependent manner. We took a simplified view of the population activity by performing dimensionality reduction with LDA, which is a supervised method to project high-dimensional dynamics onto a single axis. Specifically, through the analysis of correlated population responses across S1 and S2 along multiple LDA axes, we find that inter-areal coordination is associated with both goal-directed licking as well as whisking behavior and that it can occur independent of sensory stimuli. In the absence of tactile stimuli, $S1_{S2}$ and $S2_{S1}$ neurons do not show a special contribution to this motor-related coordination, suggesting that it does not necessarily reflect direct cortico-cortical interactions. S1 and S2 receive common input from M1 and P_{Om}, conveying efferent and re-afferent motor information (Deschenes et al., 1998; Suter and Shepherd, 2015), and are additionally coupled by thalamic relays through P_{Om} (Theyel et al., 2010) (**Figure 7**). We speculate that motor-related S1 and S2 coordination could be a result of common drive or cortico-thalamocortical pathways through these shared areas. In contrast, we find a special contribution of identified $S1_{S2}$ and $S2_{S1}$ neurons to inter-areal coordination

occurring during whisker-texture touch, indicating that their participation particularly depends on sensory stimuli. This contribution is most prominent when sensory stimuli and motor behavior are paired, such as upon licking onset on Hit trials, which further suggests that such cortico-cortical interactions could be involved in a form of “active sensation”. However, we reason that this interaction does not necessarily reflect motor behavior. Given that these neurons also specially contribute to inter-areal coordination during whisker-touch periods in CR trials, we propose that these direct cortico-cortical interactions more likely represent the exchange of sensory- or decision-related activity.

Our findings provide the first direct evidence for a unique contribution of direct cortico-cortical interactions over other sources of correlated activity across these areas. Such specificity points towards distinct but potentially synergistic roles for how different inputs may be involved in information flow across the cortex. The division between direct and indirect interactions along sensory and motor parameters, respectively, is in line with theories that indirect cortico-thalamocortical pathways are more involved in relaying motor, rather than sensory, signals (Sherman and Guillery, 2011). Additionally, both frontal cortical areas such as M1 and higher-order thalamic nuclei such as POm have been implicated in gating and coordinating activity across somatosensory areas (Pais-Vieira et al., 2013; Theyel et al., 2010; Zagha et al., 2013). In the visual system, the pulvinar, a higher-order thalamic nuclei involved in attention, has been identified in coordinating activity between visual areas (Saalmann et al., 2012). Our findings support the notion that nuclei that also drive motor-related or attention-related activity might help to coordinate primary and higher sensory areas in a manner that facilitates sensory-related direct cortico-cortical communication upon stimulus presentation.

What is the relevance of this sensory-related cortico-cortical interaction? It has been suggested that feedback inputs from higher sensory areas provide contextual information to help

extract relevant sensory features provided by feedforward inputs in primary areas (Gilbert and Li, 2013). We find that $S2_{S1}$ neurons exhibit prominent licking and decision-related activity, which is in line with recent evidence that behavior-related activity in S1 can be inherited from S2 (Yang et al., 2016). Coordinated activity between $S1_{S2}$ and $S2_{S1}$ neurons during texture discrimination may reflect sensory processing involved in several functions. One function may be associated with decision making, as exemplified by correlations increasing upon whisker touch onset and peaking upon licking onset on Hit trials. Another function may be associated with the reinforcement of particular aspects of the sensory signal that might strengthen or stabilize sensory representations through goal-directed learning, exemplified by the persistent coordinated activity after licking onset on Hit trials (Chen et al., 2015). Future work to dissect $S1_{S2}$ and $S2_{S1}$ neuronal dynamics using projection-targeted multi-area calcium imaging will help to resolve these possibilities.

In conclusion, multi-area calcium imaging with anatomical tracers presents new opportunities for overlaying functional measurements with recent comprehensive mapping of the long-range connectivity in mouse neocortex (Oh et al., 2014; Zingg et al., 2014). Several different approaches have been implemented for imaging across brain areas. While the use of multiple miniature objectives does not limit the maximum distance between areas that can be imaged (Lecoq et al., 2014), the physical size and working distance of such objectives does limit the proximity between areas and depth that can be imaged noninvasively. The use of multiple beams through a single large-FOV, long-working distance objective thus provides a complementary approach. The multi-area two-photon microscope described here shares similar design principles as reported in (Stirman et al., 2014). The core principles and modularity of these designs readily allows for improvements in temporal resolution through resonant, free-line, or random-access scanning systems (Bathellier et al., 2012; Grewe et al., 2010), increasing the

number of simultaneously imaged areas and cortical layers with low repetition rate lasers (Cheng et al., 2011; Quirin et al., 2014), and imaging across larger FOVs with different optical configurations (Stirman et al., 2014; Tsai et al., 2015).

In addition to developments in imaging technology, new genetic tools are being developed for combinatorial conditional gene expression to concurrently label increasing number of pathways (Fenno et al., 2014) and genetically encoded voltage indicators for reporting electrical signals (Akemann et al., 2013; Sun et al., 2013). These developments will expand the range of biological questions that can be addressed in elucidating the relationship between long-range cortical communication and the fine-scale organization and computations occurring within local circuitry.

Acknowledgements

We thank S. Giger, H. Kasper, and M. Wieckhorst for custom components, B. Schneider for viral reagents, P. Bethge, D. Langer, V. Mante, A. Thiele, and M. van 't Hoff for helpful discussions, J. Sanes for donating mKate antibody, H. Zeng and A. Miyawaki for the Ai92(TITL-YCX2.60) mouse, M.E. Diamond, M. Maravall, L. Pinto, and H. Safaai, for help with data analysis, and F. Collman for motion correction software. This work was supported by grants from the Swiss National Science Foundation (310030-127091; F.H.), the Swiss SystemsX.ch initiative (project 2008/2011-Neurochoice, F.H.), the US NIH BRAIN Initiative (1U01NS090475-01, F.H.), Forschungskredit of the University of Zurich (grant 541541808, J.L.C.) and a fellowship from the U.S. National Science Foundation, International Research Fellowship Program (grant 1158914, J.L.C.).

Author contributions

J.L.C., F.F.V., and F.H. devised the study; F.F.V., R.K., and J.L.C. designed and built the multi-area two-photon microscope; J.L.C. designed viral constructs and performed in vivo experiments; J.L.C. and M.J. analyzed the data; J.L.C, F.F.V., and F.H. wrote the manuscript with critical revisions from M.J. and R.K..

Author Information

Address correspondence to F.H. at helmchen@hifo.uzh.ch or J.L.C. at jerry@chen-lab.org.

Competing Interests

The authors declare no competing financial interests.

FIGURE LEGENDS

Figure 1. Multi-area two-photon microscope for flexible simultaneous imaging of sub-areas within a large field-of-view. **A**, Schematic of multi-area two-photon microscope. Light from a Ti:sapphire laser is split into two beams and one beam sent to a delay line. Each beam then enters a focal plane unit (FPU), which allows axial focusing with an electrically tunable lens (ETL). Both beams are scanned in parallel by a pair of galvo mirrors. **B**, Schematic of FPU. **C**, Imaging modes include scanning of a single large FOV (with one beam switched off) and parallel scanning of two sub-areas. **D**, Principle of spatiotemporal multiplexing: The detected fluorescence photons can be attributed to the correct area of origin by rapid demultiplexing synchronized to the laser pulse train. **E**, Example two-photon image (1.7 mm FOV) at 160-180 μm depth in a YCX2.60-expressing transgenic mouse in L2/3.

Figure 1 - figure supplement 1. Variation of the point-spread function over field-of-view position and ETL tuning range. The point-spread function (PSF) was measured using 200-nm beads (Fluoresbrite Plain YG Microspheres, Polysciences Inc) at 840 nm excitation. Off-axis positions were accessed by translating a focal plane unit (FPU) to a position corresponding to a sample-offset of 500 μm and 900 μm . Full-width-half-maxima (FWHM) of the PSF are shown for the X-, Y-, and Z-direction. The PSFs exhibit residual astigmatism and degrade when the focus is moved away from the nominal working distance ($\Delta z = 0$) and the on-axis position. Due to vignetting, the ETL tuning range is limited at 900 μm off-axis. $n = 5$ beads, error bars: 95% confidence interval.

Figure 1 - figure supplement 2. Crosstalk between both sub-areas observed in vivo. Neurons expressing YC-Nano140 were imaged with a single beam exciting fluorescence either in sub-area 1 or 2 (Average of $n = 49$ frames with motion correction). The detected signal in the non-illuminated sub-area is due to crosstalk caused by the exponential fluorescence decay (shown amplified by a factor of 10 for better visibility). The crosstalk can be quantified by the ratio of both images after background subtraction (the background was estimated from a ROI placed in the dark blood vessels). The percent crosstalk estimates are averages over 10000 pixels excluding blood vessels with standard deviation. As CFP is quenched by YFP in the Förster resonance energy transfer (FRET) interaction between both fluorophores, the lifetime of the CFP emission is shortened, which leads to a lower crosstalk.

Figure 2. Simultaneous calcium imaging of identified feedforward and feedback neurons in S1 and S2 of mouse neocortex during behavior. **A**, Viral injection scheme for simultaneous labeling of feedforward and feedback neurons and YC-Nano140 expression. **B**, Functional

mapping of S1 and S2 through optical intrinsic signal imaging. Intrinsic signals evoked by stimulation of the C2 whisker (top left) and the B2 whisker (top right). In addition to localized intrinsic signals in S1 barrel columns, additional activation spots are visible in S2. Identified barrel columns (circles) are overlaid over blood vessel (bottom left) and YC-Nano140 expression (bottom right) images. **C**, *In vivo* 2-photon images of LSSmKate2-positive S1_{S2} neurons (blue), tdTomato-positive S2_{S1} neurons (red) with non-co-labeled YC-Nano140-expressing neurons (grey) in S1 (S1_{ND}) and S2 (S2_{ND}). **D**, Behavior setup for texture discrimination task. **E**, Trial structure for go/no-go texture discrimination task. **F**, Example calcium transients for individual neurons in [C] measured episodically during texture discrimination task along with periods of whisker-to-texture touch (orange area), whisking amplitude (brown trace), and reaction time on Hit trials (green area). For each trial the selected plane in each sub-area is indicated on top, illustrating the combinatorial plane hopping.

Figure 2 - figure supplement 1. Denoising with tensor decomposition. **A**, Calcium responses from one animal across multiple sessions are organized into a data tensor. The tensor is decomposed and a low-rank tensor representing denoised calcium responses is generated. **B**, Denoising procedure: A low-rank tensor for trials and conditions was determined by cross-validation methods. A low-rank tensor for neurons was determined by convolving estimated spike trains from experiment data to generate simulated calcium traces. Noise is added to simulate calcium traces and tensor decomposition is performed to determine an optimum low-rank tensor by comparing simulated vs. simulated denoised traces. Once an optimum low rank tensor is determined for all dimensions, tensor decomposition is applied to raw traces. **C**, Low tensor rank (arrow) computed by cross-validation of training set. **D**, Contribution of each dimension to low tensor rank in [C]. **E**, Final low tensor rank offset (arrow) computed by cost

function of simulated vs. simulated denoised traces. **F**, Comparison of simulated traces denoised with tensor decomposition vs. Gaussian filter. **G**, Denoised fits from Gaussian filter vs. tensor decomposition for single neurons from simulated data. **H**, Example of experimental data before and after denoising. **I**, Optimum T' or $N' + N'_{\text{offset}}$ vs. active neurons for each animal.

Figure 2 – Source data file 1. Optimized low tensor rank across animals. Table of optimum column size of each factor matrices related to neurons ($N' + N'_{\text{offset}}$), time points (T'), and trial conditions (C') determined after cross-validation and cost function procedures for each animal used for denoising. Total possible column sizes are also indicated along with number of active neurons.

Figure 3. Feedback neurons in S2 exhibit behavior-related responses. **A**, General linear model (GLM) of behavior-related responses. Example of GLM fit for one neuron of calcium responses against touch, licking, and whisking as behavior events. Single-trial calcium responses are plotted along with model fit as well as touch periods with onset indicated, individual licks with onset indicated, whisking envelope amplitude, and decision. **B**, GLM coefficients (B) for example neuron shown in [A] for regressors for touch onset, whisking envelope amplitude, and licking onset across different delays. Delays are aligned to the onset of each behavioral event. **C**, Cumulative probability distribution (cpd) of overall GLM fit across cell types. **D**, GLM coefficients for different cell types for regressors for touch onset (left), whisking envelope amplitude (middle), and licking onset (right) across different delays. Grey line indicates average GLM coefficient for neurons with non-significant coefficients at that time point. **E**, Fraction of active neurons able to discriminate Hit vs. CR, FA vs. CR, and P280 vs. P1200 trials above

chance determined by single-cell ROC analysis. (shaded area: s.e.m. error bars: s.d. from bootstrap test; $n = 44$ S1_{S2}, 161 S1_{ND}, 59 S2_{S1}, 198 S2_{ND} neurons).

Figure 3 - figure supplement 1. General linear model of whisking- and licking-related calcium responses. **A-B**, Example of GLM fit for neurons showing prominent whisking [A] and licking [B] related calcium responses against touch, licking, and whisking behavior events. Single-trial calcium responses are plotted along with model fit as well as touch periods with onset indicated, individual licks with onset indicated, and whisking envelope amplitude. **C-D**, GLM coefficients (B) for neurons in [A] and [B], respectively, for regressors for touch onset, whisking envelope amplitude, and licking onset across different delays. Delays are aligned to the onset of each behavioral event.

Figure 4. Illustration of extracting population response time courses by linear discriminant analysis. **A**, While LDA is performed on multiple simultaneously imaged neurons, for demonstration purposes, here calcium transients of two simultaneously imaged neurons within an imaging plane are plotted and sorted according to Hit and CR trials. Dotted line indicates whisker-touch onset. **B**, Example linear discriminant analysis performed on the two neurons in [A]. Bottom panel shows scatter plot of trial-by-trial responses for each neuron at the indicated time point (red region in [A]) rotated along the LD axis for Hit vs. CR trials. Top panel shows distribution of trials for population activity projected along the LD axis along with mean LD response. **C**, Average S1 or S2 population responses after LDA in Hit and CR trials across the first second prior to and following whisker-touch onset. **D**, ROC analysis of S1 or S2 population responses shown in [C] for Hit vs. CR trials under task conditions demonstrating the performance

of the LDA. Dotted line indicates touch onset. (shaded area: s.e.m.; $n = 21$ S1 planes, 21 S2 planes).

Figure 5. Motor behavior is associated with coordinated population activity across S1 and

S2. A, Analysis of coordinated activity across S1 and S2. Left panel shows example of single-trial population responses for Hit trials projected along Hit vs. CR axis for simultaneously imaged S1 (LD_{S1}) and S2 (LD_{S2}) of S2 sub-areas. Upper right panels shows trial-by-trial correlations ($LDCC_{S1:S2}$) between LD_{S1} and LD_{S2} at indicated time points. Bottom right panel shows calculated $LDCC_{S1:S2}$ across the trial period. **B,** $LDCC_{S1:S2}$ for Hit vs. CR trials. **C,** Normalized histogram of reaction times across Hit trials. **D,** $LDCC_{S1:S2}$ for Hit trials along Hit vs. CR axis aligned to licking onset. **E,** $LDCC_{S1:S2}$ for FA vs. CR trials. **F,** Licking rate for FA trials in which licking onset precedes (pre-wo) and follows (post-wo) whisker-touch onset. **G,** $LDCC_{S1:S2}$ for pre-wo vs. post-wo FA trials. **H,** High vs. low whisking amplitude CR trials. **I,** $LDCC_{S1:S2}$ for high vs. low whisking amplitude CR trials. All time course data are aligned to whisker-touch onset (black dotted line, x-axis) except for [D] which is aligned to licking onset (red dotted line). shaded area: s.e.m.; (C,D,E,G,I) $n = 63$ pairs of S1 and S2 planes in 7 animals; (C) $n = 7120$ trials (F) $n = 1120$ trials (H) $n = 7$ animals, 6960 trials.

Figure 5 - figure supplement 1. Linear discriminant analysis across different sensory or

behavior axes. Average S1 or S2 population responses across the first second prior to and following whisker touch onset for: **A,** FA vs. CR trials; **C,** high vs. low amplitude whisking CR trials; **E,** target vs. non-target textures under non-task conditions; **G,** P280 vs. P1200 textures for CR trials. ROC analysis of S1 or S2 population response for: **B,** FA vs. CR trials; **D,** high vs. low amplitude whisking CR trials; **F,** target vs. non-target textures under non-task conditions; **H,**

P280 vs. P1200 textures for CR trials. Dotted line indicates touch onset. (shaded area: s.e.m.; n = 21 S1 planes, 21 S2 planes)

Figure 5 - figure supplement 2. Coordinated activity across S1 and S2 is not stimulus-specific. **A**, $LDCC_{S1:S2}$ for target vs. non-target textures under non-task condition trials. **B**, $LDCC_{S1:S2}$ for P280 vs. P1200 textures for CR trials. We observe no increased or different $LDCC_{S1:S2}$ between target and non-target textures under non-task conditions when animals received sensory stimulation but neither whisked nor licked. We also observed no increase or difference in $LDCC_{S1:S2}$ when analyzing population responses for P280 vs. P1200 textures on CR trials under task conditions. All time course data are aligned to whisker-touch onset (black dotted line, x-axis). shaded area: s.e.m.; n = 63 pairs of S1 and S2 planes in 7 animals.

Figure 6. Projection neurons contribute to coordinated S1 and S2 activity. **A**, The contribution of specific cell types to coordinated activity across S1 and S2 is measured by trial-shuffling responses for those cell types prior to calculating the $LDCC_{S1:S2}$. The resulting $LDCC_{S1:S2}$ from the shuffled condition is then subtracted by the $LDCC_{S1:S2}$ from the control condition to obtain $\Delta LDCC_{S1:S2}$ (see also Figure 6-figure supplement 1). **B**, $\Delta LDCC_{S1:S2}$ for Hit trials along the Hit vs. CR axis after aligning to licking onset. **C**, $\Delta LDCC_{S1:S2}$ for high-amplitude whisking CR trials along the high vs. low whisking amplitude CR trial axis. **D**, $\Delta LDCC_{S1:S2}$ for FA trials, in which licking onset precedes whisker-touch onset along the FA vs. CR axis. **E**, $\Delta LDCC_{S1:S2}$ for FA trials, in which licking onset follows whisker-touch onset along the FA vs. CR axis. **F**, $\Delta LDCC_{S1:S2}$ for CR trials along the FA vs. CR axis. All time course data are aligned to whisker-touch onset (dotted line, x-axis) except for [B] which is aligned to licking onset (red

dotted line). (shaded area: s.e.m.; $n = 21$ S1 planes, 21 S2 planes, 63 pairs of S1 and S2 planes in 7 animals).

Figure 6 - figure supplement 1. Measuring the contribution of specific cell types to coordinated population activity. **A**, An example of population response after trial shuffling. Trial responses of neuronal subpopulations were shuffled in order to determine their contribution to the population response. For the two example neurons also shown in [Figure 4A, B], the contribution of 'cell 2' on the population response for Hit trials was examined by shuffling the order of trial responses for 'cell 2'. A scatter plot of the trial-by-trial responses of 'cell 1' vs. 'cell 2' is shown before (middle) and after (bottom) shuffling. The corresponding trials in control and shuffled conditions are indicated by color. The population responses under shuffled conditions were projected onto the LD axis for Hit vs. CR trials determined under control conditions (top). **B**, Example analysis of coordinated activity across S1 and S2 after trial shuffling. Single-trial population responses for CR trials projected along the FA vs. CR axis for simultaneously imaged S1 (LD_{S1}) and S2 (LD_{S2}) sub-areas are shown under control conditions (top left) and after shuffling trials of $S1_{S2}$ and $S2_{S1}$ neurons (top right). Bottom panel shows trial-by-trial correlations ($LDCC_{S1:S2}$) between LD_{S1} and LD_{S2} at indicated time point for control and shuffled conditions. See [Figure 6A, B] for subsequent analysis of the same sub-areas to measure $\Delta LDCC_{S1:S2}$ across the trial period.

Figure 6 - figure supplement 2. Projection of shuffled trials does not alter average population response. **A**, Cumulative distribution of average peak calcium responses for each cell type. **B**, Average S1 (top) or S2 (bottom) population responses projected along the Hit vs. CR axis across the first second prior to and following whisker-touch onset in data in which no

trials are shuffled (control), trials of $S1_{S2}$ and $S2_{S1}$ neurons are shuffled ($S1_{S2}S2_{S1}$), and $S1_{ND}$ and $S2_{ND}$ neurons are shuffled ($S1_{ND}S2_{ND}$). **C**, ROC analysis of S1 (top) or S2 (bottom) population responses, in which no trials are shuffled (control), trials of $S1_{S2}$ and $S2_{S1}$ neurons are shuffled ($S1_{S2}S2_{S1}$), and $S1_{ND}$ and $S2_{ND}$ neurons are shuffled ($S1_{ND}S2_{ND}$) vectors for Hit vs. CR trials under task conditions. Dotted line indicates touch onset. (shaded area: s.e.m.; $n = 21$ S1 planes, 21 S2 planes).

Figure 6 - figure supplement 3. Contribution of $S1_{S2}$ and $S2_{S1}$ neurons to Hit and CR trials relative to whisker-touch onset. **A**, Contribution of $S1_{S2}$ and $S2_{S1}$ neurons or $S1_{ND}$ and $S2_{ND}$ neurons to coordinated S1 and S2 activity for Hit trials along the Hit vs. CR axis after aligning to whisker-touch onset (dotted line). **B**, Contribution of $S1_{S2}$ and $S2_{S1}$ neurons or $S1_{ND}$ and $S2_{ND}$ neurons to coordinated S1 and S2 activity for Hit trials along the Hit vs. CR axis after aligning to whisker-touch onset. (shaded area: s.e.m.; $n = 63$ pairs of S1 and S2 planes in 7 animals).

Figure 7. Model of coordinated activity across S1 and S2. Our results identify coordinated activity patterns across S1 and S2 that are related to motor behaviors, which could arise from common input from M1 or POm or indirect cortico-thalamocortical (CTC) pathways through POm. $S1_{S2}$ and $S2_{S1}$ neurons especially participate in inter-areal coordination when motor behavior is paired with sensory stimuli suggesting that such cortico-cortical (CC) interactions specifically reflect the exchange of sensory information during active sensation.

Table 1. Axes used for linear discriminant analysis. Summary of trial conditions compared and used for linear discriminant analysis. For each axes, noted are potential differences in

texture, licking, and whisking parameters between trial conditions as well as the utility in comparing such trial conditions for isolating sensory or behavior responses.

Axes for LDA	Texture	Licking	Whisking	Utility in Analysis
Hit vs. CR	Different	Different (Hit)	Same	Cannot isolate sensory, decision, or action-related responses
FA vs. CR	Same	Different (FA)	Same	Isolate decision and action-related responses
Pre- vs. post-touch licking (FA trials)	Same	Different	Same	Isolate licking-related responses
High vs. Low Whisking (CR trials)	Same	None	Different	Isolate whisking-related responses
P280 vs. P1200 (CR trials)	Different	None	Same	Isolate sensory-related responses
Target vs. Non-target (Non-task)	Different	None	None	Isolate sensory-related responses

Video 1. *In vivo* z-stack of YC-Nano140 expressing neurons. Single area images from the multi-area two-photon microscope of L2/3 neurons were taken from 70-210 μm below the pial surface at 1 μm z-step resolution. Sub-area excitation beam was delivered through the ETL, positioned either on-axis (left) or 900 μm off-axis (right), and focusing was achieved through positioning of objective by mechanical z-stage.

Video 2. Simultaneous calcium imaging across S1 and S2. Single trial video of calcium responses during texture discrimination acquired at 7Hz with the multi-area two-photon microscope (1x playback speed). YFP (green) and CFP (blue) fluorescence from YC-Nano140 are shown and overlaid with calculated $\Delta R/R$ (red).

662

663 MATERIALS AND METHODS

664

665 **Multi-area two-photon microscope.** The microscope consists of several building blocks: The
666 beam preparation stage, which sends two pulse trains with the correct delay and intensity to the
667 focal plane units (FPUs), which in turn allow independent focusing and positioning of each sub-
668 area. The scan system scans the beams directed to each sub-area in parallel and sends them to the
669 objective via the excitation optics. The microscope front end consists of the objective, z-stage and
670 detection system. FPUs, excitation optics and the microscope front end were mounted on an
671 elevated breadboard. The optical design software Zemax (Zemax LLC, Redmond, USA) was
672 used for system layout and performance evaluation.

673 **Beam preparation.** Laser light from a Ti:sapphire laser (Mai Tai HP DeepSee, Spectra-Physics)
674 was split into two beams using a 50:50 femtosecond beam splitter (10RQ00UB.4, Newport). In
675 each beam path, a Pockels cell (Model 350-80-LA-02, Conoptics, Danbury, CT) was used to
676 adjust the laser intensity. A 4x beam expander composed of a -25 mm and 100 mm achromat
677 (ACN127-25B and AC254-100B-ML, Thorlabs) was matched to the beam size to the FPU
678 entrance aperture. An adjustable delay line was implemented for one beam path to allow tuning
679 of the relative phase of both excitation beams.

680 **Focal plane units.** The two focal plane units were built in mirrored design from opto-mechanical
681 parts on 200x450 mm breadboards (MB2060/M, Thorlabs) mounted on linear translation stages
682 (Standa 8MTF-102LS05, Vilnius, LT) with kinematic seats (KBS98B, Thorlabs) to allow for
683 quick exchange of FPU configurations. For focusing each FPU contained an electrically tunable
684 lens (Optotune EL-10-30-C, selected for low wavefront aberrations, focal length tuning range: 80
685 to 230 mm, Optotune AG, Zurich, CH), positioned in a plane conjugate to the scanners and
686 coupled to the first scan lens via a relay lens (Thorlabs AC254-125-B-ML) and a small fold

mirror (Thorlabs MRA10-E03). For tuning the beam from convergent to divergent (equivalent to decreasing or increasing the working distance of the objective, respectively), each ETL was combined with a negative offset lens ($f = -120$ mm, Qioptiq). In each FPU a relay lens (Thorlabs AC254-125-B-ML) and a small fold mirror (Thorlabs MRA10-E03) was used to direct the beam into the scan system.

Scan system. The output beams from the two FPUs were coupled into the scan system which consisted of two identical scan lenses (S4LFT0089/98, Sill Optics, Wendelstein, D) via the cantilever arms. XY-movement of the FPUs and ETL-focusing enabled independent positioning and focusing of the two imaging sub-areas for the two beams. 6-mm galvanometric scan mirrors were used in the scan unit (6215H, Cambridge Technology, Bedford, MA).

Excitation optics. A 200 mm tube lens (AC508-200B, Thorlabs) coupled the excitation beams into the microscope objective (16X CFI75 LWD (NA 0.80), Nikon, Egg, CH). With 6-mm scan mirrors, the effective excitation NA was 0.53, which under-filled the microscope objective.

Microscope front end. The objective and the detector system were mounted on a custom-made Z-translation stage with high load capacity (Feinmess LT235-50-DC-R-B, Dresden, Germany). A crossed-roller ring bearing (THK RU178UCC0G, Tokyo, Japan) allowed the rotation of the Z-stage, objective and detection system to accommodate for different tilts of the cover slip of the chronic window preparation.

Detection optics and electronics. The detection system of the microscope was optimized for high detection efficiency over large FOVs by making use of the large acceptance angles of the hybrid photo detectors (HPDs, R11322U-40 MOD, Hamamatsu). To de-magnify the 20 mm-pupil of the microscope objective onto the 5 mm-active area of the HPDs, we used a 4.7x telescope composed of a 90 mm-Achromat (G322389000, Qioptiq) and a wide-angle eyepiece (Panoptic 19 mm, TeleVue). A dichroic mirror (515DCXR, Chroma Technologies) located

between the achromat and eyepiece split the emission light into two channels in which blue (480/60 nm, Semrock) and yellow (542/50 nm, Semrock) emission filters and IR rejection filters (FF01-720/SP-25, Semrock) were located. The HPD signal was preamplified (C1077B, Hamamatsu) and digitized by an analog-to-digital converter (ADC, NI-5771, National Instruments) connected to a field-programmable array (FPGA, NI-7962R, National Instruments). For synchronizing the data acquisition to the laser pulse train (Cheng et al., 2011), the signal of the internal reference photo diode of the laser was sent to an adjustable electronic delay line (DB64, Stanford Research Systems) and amplified (BBA100VG, Alphalas) before being fed into the trigger line of the ADC. The FPGA counted the pulses arriving from the two excitation beams and sorted the resulting HPD emission signal accordingly in order to separate the images acquired from two sub-areas at a rate of 160 MHz.

Microscope software. For microscope control, a custom-written software ‘SCOPE’ was programmed in C++ (Visual Studio C++) and used control live scanning, data acquisition, laser intensity, FPU and ETL movement, and the synchronization to other experimental equipment. For combinatorial plane hopping during behavior experiments, custom behavior software programmed in LabVIEW was used to trigger multi-area imaging through SCOPE and control laser intensity and ETL focus shift. Documentation is available at <http://rkscope.sourceforge.net/>.

Generation of viral construct. For construction of the *AAV-EF1 α -fio-H2BLSSmKate2* viral construct, the double-inverse oriented FRT (*fio*) sites was synthesized *de novo* (GenScript) with flanking *Bam*H1 and *Eco*RI restriction sites and an internal *Asc*I and *Nhe*I sites and insert into an *AAV-EF1 α -YC-Nano140* (Chen et al., 2013b) backbone plasmid. The *H2B* subunit with 5' *Nhe*I and 3' *Age*I restriction sites was generated by PCR amplification from a *pTagRFP-H2B* vector (Evrogen) and subcloned into an *pLSSmKate2-N1* plasmid (Piatkevich et al., 2010).

Subsequently, *H2BLSSmKate2* with 5' *NheI* and 3' *AscI* restriction sites was generated by PCR amplification followed by insertion into the *AAV-EF1 α -fio* plasmid. The *AAV-syn-Flpe* viral construct was generated by restriction enzyme digest of *pCAG-Flpe*(Matsuda and Cepko, 2007) and insertion into the *pAAV-6P-SEWB* backbone plasmid. For the *AAV-EF1 α -dio-NLStdTomato* viral construct, *NLStdTomato* with 5' *NheI* and 3' *AgeI* restriction sites was generated by PCR amplification from a *pTagRFP-H2B* vector followed by insertion into the *AAV-EF1 α -dio-eYFP* plasmid. The *AAV-pgk-Cre* construct was previously described³. Recombinant serotype 6 AAV particles were produced by co-transfecting AAV-293 cells with the shuttle plasmid and the pDP6 packaging plasmid. Recombinant serotype 1 AAV particles were produced by co-transfecting AAV-293 cells with the shuttle plasmid and the pDF1 packaging plasmid. Cell lysates were subjected to purification on iodixanol density gradients followed by HPLC with HiTrap Heparin column for AAV2 or by anion exchange HPLC for AAV1 (GE Healthcare Bio-Sciences AB) using standard procedures. The viral suspension obtained was concentrated using Centricon® centrifugal filter devices with a molecular weight cut-off of 100 kDa (Millipore, Billerica, MA), and the suspension medium replaced with PBS. Vector titres were determined by measuring the number of encapsidated genomes per ml by real-time PCR.

Viral injections and cranial window implantation. Experimental procedures followed the guidelines of the Veterinary Office of Switzerland and were approved by the Cantonal Veterinary Office in Zurich. Stereotaxic viral and tracer injections were performed on young adult (P35-42) male wild type C57Bl6/J mice as previously described (Chen et al., 2013b). A solution containing AAV1-*EF1 α -YC-Nano140*, AAV1-*EF1 α -fio-H2BLSSmKate2*, and AAV6- *pgk-Cre* (200 nl total volume, $\sim 1 \times 10^9$ vg/ μ l per virus, 2:1:1 ratio by volume) was delivered into S1, targeting L2/3 and L5 (~ 300 and 500μ m below the pial surface). A solution containing AAV1-

EF1 α -YC-Nano140, AAV1-*EF1 α -dio-NLStdTomato*, and AAV6-*syn-Flpe* (200 nl total volume, $\sim 1 \times 10^9$ vg/ μ l per virus, 2:1:1 ratio by volume) was delivered into S2, targeting L2/3 and L5 (~ 300 μ m and 500 μ m below the pial surface). Injection regions were selected by optical intrinsic signal imaging or stereotaxic coordinates (1.1 mm posterior to bregma, 3.3 mm lateral for S1; 0.7 mm posterior to bregma, 4.2 mm lateral for S2). To allow long-term *in vivo* calcium imaging, a cranial window was implanted 24 hrs after virus injections over S1 as described³³. A metal post for head fixation was implanted on the skull, contralateral to the cranial window, using dental acrylic. For demonstration of large single-FOV imaging, structural images were acquired from one adult male *Rasgrf2-2A-dCre;Camk2atTA;Ai92(TITL-YCX2.60)* transgenic mouse (Madisen et al., 2015) implanted with a cranial window without viral injections.

Animal behavior. Mice were housed 2-3 per cage in reverse 12-hr light cycle conditions. All handling and behaviour occurred under simulated night time conditions. One week following chronic window implantation, mice were handled daily for 1 week while acclimated to a minimum of 15 minutes of head fixation. Mice were water restricted and trained to a go/no-go texture discrimination task previously described (Chen et al., 2013b). Imaging during behaviour began following 3-5 training sessions once animals reached a performance level of $d' > 1.75$ (80% correct) for one session. Imaging under task conditions was performed over the course of 5-6 sessions at a performance level of $d' = 2.62 \pm 0.15$. Once sufficient task-related data was acquired, mice were provided with free access to water and then imaged for an additional 5-6 sessions under non-task conditions, in which textures were presented but no reward or punishment delivered. Sample sizes were chosen based on previous behavioural imaging studies, which comprise 6–10 mice per group (Chen et al., 2013b; Chen et al., 2015). Due to their low occurrence ($6.7 \pm 0.5\%$ of all trials), miss trials were excluded from analysis. No statistical

methods were used to predetermine sample size. Since animals constitute a single experimental group, no randomization of animals or blinding to experimenter was performed.

Intrinsic signal optical imaging. The S1 and S2 barrel column was identified using intrinsic signal optical imaging under ~1.5% isoflurane anaesthesia. The cortical surface was illuminated with 630-nm LED light, single whiskers were stimulated (2-4° rostro-caudal deflections at 10 Hz), and reflectance images were collected through a 4x objective with a CCD camera (Toshiba TELI CS3960DCL; 12-bit; 3-pixel binning, 427x347 binned pixels, 8.6-μm pixel size, 10-Hz frame rate). Intrinsic signal changes were computed as fractional changes in reflectance relative to the pre-stimulus average (50 frames; expressed as $\Delta R/R_{IOS}$). Barrel column centres for stimulated whiskers were located by averaging intrinsic signals (15 trials), median-filtering (5-pixel radius), and thresholding to find signal minima. Reference surface vasculature images were obtained using 546-nm LED illumination and matched to images acquired during 2-photon imaging. Prior to behavior training, all whiskers excluding the principal and first-order surround whiskers corresponding to the expression area were partially trimmed to a length out of reach from texture contact during the task. During whisker trimming, the principal whisker was noted by images taken from the high-speed video camera for re-identification in subsequent imaging sessions for whisker tracking.

Whisker tracking. The whisker field was illuminated with 940-nm infrared LED light and movies were acquired at 500 Hz (500x500 pixels) using a high-speed CMOS camera (A504k; Basler). Average whisker angle across all imaged whiskers was measured using automated whisker tracking software (Knutsen et al., 2005). Because our limited temporal resolution of imaging (7 Hz) precluded analysis of rapid dynamics within individual whisking cycles, we

based our analysis on the envelope amplitude of whisking calculated as the difference in maximum and minimum whisker angle along a sliding window equal to the imaging frame duration (142 ms). The slower dynamics of the envelope amplitude represents both rhythmic and non-rhythmic forms of whisking behavior. For comparison between high- vs. low-amplitude whisking trials, the mean whisking amplitude during the 1-s period prior to whisker-touch onset was calculated for each animal and high- and low-amplitude trials were identified as those whose amplitude during the same period was greater or less than the mean, respectively. For all trials, the first and last possible time point for whisker to texture contact was quantified manually through visual inspection.

Identification of feedforward and feedback neurons. For *in vivo* identification of LSSmKate-positive feedforward and tdTomato-positive feedback neurons, 3D-volume image stacks were taken on a standard custom-built 2-photon microscope controlled by HelioScan³⁴, equipped with a Ti:sapphire laser system (~100-fs laser pulses; Mai Tai HP; Newport Spectra Physics), a water-immersion objective (40×LUMPlanFI/IR, 0.8 NA; Olympus), galvanometric scan mirrors (model 6210; Cambridge Technology), and a Pockels Cell (Conoptics) for laser intensity modulation. An 800-nm excitation with 610/75 nm emission filter and 840-900 nm excitation with 697/75 nm emission filter was used for tdTomato and LSSmKate2, respectively.

Due to suboptimal *in vivo* 2-photon excitation of LSSmKate2, additional H2BLSSmKate2-positive neurons were identified followed by antibody staining of LSSmKate2 for signal amplification. Mice were anesthetized (ketamine/xylazine; 100/20 mg/kg body weight) and perfused transcardially with 4% paraformaldehyde in phosphate buffer, pH 7.4. Cortical sections (50 μ m) were cut along the imaging plane using a vibratome (VT100; Leica), then blocked in 10% NGS and 1% Triton at room temperature and incubated overnight at 4°C in 5%

NGS, 0.1% Triton and mKate guinea pig polyclonal antibody(Cai et al., 2013); 1:1,000). A guinea pig Alexa647–conjugated goat IgG secondary antibodies (1:400; Molecular Probes, Invitrogen) was applied for 2 hrs at room temperature. Images were acquired with a confocal microscope (Fluoview 1000; Olympus), green (YC-Nano140), red (tdTomato), and infrared (Alexa647) excitation/emission filters.

Calcium imaging analysis. Two-channel, two-area (CFP/YFP) calcium imaging data was imported into MATLAB (Mathworks) for processing. For each channel, spatial linear unmixing was applied for the two area as described below. Background was subtracted on each area and channel (bottom 1st percentile fluorescence signal across entire frame). For each area, Hidden Markov Model line-by-line motion correction was applied to both data channels³⁷. Regions of interests (ROIs) corresponding to individual neurons were manually selected from the mean image of a single-trial time series using ImageJ (National Institute of Health). Mean pixel value for each ROI was extracted for both channels. Calcium signals were expressed as relative YFP/CFP ratio change $\Delta R/R = (R - R_0)/R_0$. R_0 was calculated for each trial as the bottom 8th percentile of the ratio for the trial. Active neurons were identified by two-way ANOVA with repeated measures of the neuronal calcium signal against the neuropil signal (significance value, $P < 0.05$) for each imaging session. The neuropil is defined as a region of interested selected from the entire imaging frame representing non-somatic tissue expressing YC-Nano140 but excluding blood vessels.

Denoising with tensor decomposition. Calcium signals were denoised using tensor decomposition before further analysis (**Figure 2-figure supplement 1 and source data file 1**) (Cong et al., 2015; Seely et al., 2014). Tensor decomposition is a method used for dimensionality

reduction, which can be viewed as a generalization of singular value decomposition of data represented as tensors rather than matrices (Hitchcock, 1927). While calcium imaging recordings are often described as two-dimensional matrices comprised of neurons and time dimensions, it can additionally be described along a third dimension representing trial conditions (**Figure 2-figure supplement 1A**). For such data, tensor decomposition can be used as a form of single-trial denoising by assuming that calcium signals across neurons, time, and trial conditions are not independent and that multi-linear relationships across dimensions therefore can be exploited. Through tensor decomposition, background noise that does not match the assumed multi-linear structure can be reduced if present. Single-trial denoising of calcium transients is desirable when analyzing conditions with low trial counts such as FA trials (7.4% of all trials) in order to improve statistical analysis of such conditions.

For each animal, calcium signals were arranged into a data tensor (Y) across three dimensions according to the number of trial conditions (I ; i.e., 6 combinations of decision and texture), number of neurons (J), number of time points (K). Using Tucker decomposition, this tensor can be described elementwise as:

$$y_{ijk} = \sum_{c=1}^C \sum_{n=1}^N \sum_{t=1}^T g_{cnt} m_{ic} m_{jn} m_{kt} \quad \text{for } i = 1 \dots I, j = 1 \dots J, k = 1 \dots K \quad (1)$$

consisting of a factor matrix related to trial-condition containing elements (m_{ic}) with column size C , a factor matrix related to neuron containing elements (m_{jn}) with column size N , a factor matrix related to time point (m_{kt}) with column size T , and a core tensor describing the interactions between the matrix components containing elements (g_{cnt}). From this, a low rank tensor, Y' , containing the denoised traces can be described elementwise as:

$$y'_{ijk} = \sum_{c=1}^{C'} \sum_{n=1}^{N'} \sum_{t=1}^{T'} g_{cnt} m_{ic} m_{jn} m_{kt} \quad \text{for } i = 1 \dots I, j = 1 \dots J, k = 1 \dots K \quad (2)$$

This tensor is obtained by reducing the column size of each factor matrices across each dimension resulting in C' which is related to the number of trial conditions such that ($C' \leq I$), N' which is related to the number of neurons such that ($N' \leq J$), and T' which is related to the number of time points such that ($T' \leq K$). From this, a tensor rank (θ') for Y' can be expressed as the sum of the reduced column sizes across all dimensions:

$$\theta' = C' + N' + T' \quad (3)$$

In order to determine the optimum θ' , a 5-fold cross validation procedure was first performed (**Figure 2-figure supplement 1B**) (Seely et al., 2014). For each trial condition in each neuron, trials were divided into a training set (80% of trials) and a test set (20% of trials). Single-trial traces in each tensor element were replaced with average traces from the training set. Denoised traces were obtained for a given θ' and compared to the average traces of the test set by computing the mean squared errors (MSE) (**Figure 2-figure supplement 1C,D**). The optimum θ' is identified as θ' with the minimum MSE . Determining θ' by 5-fold cross validation is advantageous in that it is unsupervised and can correct for unknown sources of noise. However, since the error estimation used in this procedure is based on comparing average traces, the θ' determined is not necessarily optimized for denoising single-trial responses and thus neurons with variable trial-to-trial responses may not be properly denoised. Indeed, while 5-fold cross validation was sufficient in identifying optimum θ' for T' and C' , better fits for some neurons were observed when manually adjusting N' (data not shown).

In order to improve denoising of single-trial responses, a second-step procedure was implemented to optimize N' through a supervised approach of performing tensor decomposition on noisy simulated calcium transients in order to determine a rank offset (N'_{offset}) resulting in a final tensor rank (θ'_{final}) such that:

$$\theta'_{final} = C' + N' + N'_{offset} + T' \quad (4)$$

where the denoised transient best reflects the ideal transients.

In order to emulate the multi-linear structure across neurons, time, and trial conditions present in our experimental data that is required for tensor decomposition, a peeling algorithm (Grewe et al., 2010) using previously measured YC-Nano140 parameters (Chen et al., 2013) (single-action potential transient: $A_0 = 4.54\%$, $\tau_{onset} = 0.186$ s, $A_{peak} = 2.3\%$, $\tau_{decay} = 0.673$ s) was applied to raw traces to extract estimated spike trains for all neurons and trials for a single animal. While the accuracy and precision of the estimated spikes may vary depending on noise in the raw trace (Lütcke et al., 2013), the multi-linear relationships across each tensor dimension is preserved. The estimated spike trains are then convolved using YC-Nano140 parameters to produce ideal simulated calcium transients. The degree of noise under experimental conditions is estimated by assuming that any variance in calcium signal present in inactive neurons reflects non-neuronal noise. For each inactive neuron, a normal distribution was fit to raw calcium traces to obtain σ representing the degree of noise for that neuron. Noise was then added neuron-by-neuron to simulated calcium transients that matched the σ 's from all inactive neurons in the data set.

The similarity between the ideal and denoised simulated trace was measured by computing the Pearson's correlation coefficient (CC) between the two traces for each neuron and taking the average across neurons. From this, the optimum θ'_{final} was determined by calculating a cost function representing the difference between θ'_{final} and the CC obtained from θ'_{final} , each normalized across the range of tested θ'_{final} :

$$Cost(\theta'_{final}) = \|\theta'_{final}\| - \|CC(\theta'_{final})\| \quad (5)$$

such that the optimum θ'_{final} resulted in the minimum $Cost(\theta'_{final})$ (**Figure 2-figure supplement 1E**).

In comparing denoising of simulated transients with tensor decomposition against temporal smoothing by a 5-point Gaussian filter, we observed that denoising with tensor decomposition better preserves the onset and peak of calcium transients, resulting in better *CC* of denoised to ideal traces (Tensor decomposition 0.69 ± 0.01 , Gaussian filter: 0.65 ± 0.01 , $P < 1 \times 10^{-6}$, Student's *t*-test, **Figure 2-figure supplement 1F,G**). This suggests that denoising with tensor decomposition is preferred when investigating sub-second temporal dynamics of activity as it preserves high frequency components of the calcium signal.

The optimum θ'_{final} for each animal was determined for denoising (**Figure 2-figure supplement 1H**). We asked if the size of the optimum low rank tensor used for denoising was similar across animals (**Figure 2-source data file 1**). We observed that C' was largely consistent across animals and reflected a rank near the total possible ranks along the condition dimension. For T' and $N' + N'_{offset}$, we observed that the optimum column size across these dimensions was strongly correlated with the number of identified active neurons (T' : $R = 0.82$, $P < 0.05$; $N' + N'_{offset}$: $R = 0.82$, $P < 0.05$, Pearson's correlation, **Figure 2-figure supplement 1I**). This suggests that the optimum low rank tensor identified for denoising captures a relevant portion of the original data tensor containing real calcium transient events.

Spatial linear unmixing. Spatial linear unmixing is based on the fact that the total PMT signal recorded at the corresponding pixel for both areas in a given channel is the linear sum of the signal for each area weighted by the cross talk resulting from the fluorescence lifetime of the indicator. For a dual beam system, the contribution of the two detected areas can be represented by the following equations:

$$J_1(x,y) = s_{1,1} \times I_1(x,y) + s_{1,2} \times I_2(x,y) \quad (6)$$

$$J_2(x,y) = s_{2,1} \times I_1(x,y) + s_{2,2} \times I_2(x,y)$$

where J is the total signal per area, I is the fluorophore abundance, and S is the crosstalk. These equations can be expressed as a matrix:

$$[J] = [S] [I] \quad (7)$$

whereby the unmixed image $[I]$ can be calculated using the inverse matrix of $[S]$:

$$[I] = [S]^{-1} [J] \quad (8)$$

Assuming the detected signal in both areas represents the total signal:

$$s_{1,1} + s_{2,1} = 1 \quad (9)$$

$$s_{1,2} + s_{2,2} = 1$$

$[S]$ was determined empirically at the beginning of each session using the experimentally prepared mouse expressing YCNano140. The intended FOVs were sequentially scanned with a single excitation beam during dual area acquisition mode. The resulting crosstalk into each area was calculated from the acquired reference images and applied for spatial linear unmixing of subsequent dual beam data using MATLAB.

Behavior classification. Behavior-related activity was described using a general linear model (GLM) (Miri et al., 2011; Pinto and Dan, 2015) expressed as:

$$Y_t = \sum_{i=-3}^6 B_i^L X_{t-i}^L + \sum_{i=-3}^6 B_i^W X_{t-i}^W + \sum_{i=-3}^6 B_i^T X_{t-i}^T \quad (10)$$

Z-scored regressors (X_{t+i}) representing touch onset (T), whisking envelope amplitude (W), and licking onset (L) with regression coefficients (B_i) at different delays (i) were used to model the z-scored calcium signal (Y_t) across time frames t . Regressors for touch onset and whisking amplitude were obtained from the whisker-tracking video while regressors for licking onset were obtained from the lick-sensor data. Each regressor was down sampled to match the calcium imaging frame rate. Touch onset was selected to best reflect touch-related responses given

previously reported neuronal adaptation in neuronal firing upon repeated touches (Musall et al., 2014; Yamashita et al., 2013). Whisking envelope amplitude was previously observed to best reflect periods of whisking and non-whisking behavior in order to identify whisking-related neurons (Chen et al., 2013b). Given the slow kinetics of calcium indicators and given that the imaging rate is well below the Nyquist rate of the natural whisking frequency (~10 Hz) (Kleinfeld and Deschenes, 2011), whisking-related signals measured here do not reflect whisking frequency. Licking onset was selected due to the observation that licking behavior in task-performing mice typically proceeds in licking bouts. Introducing additional behavioral regressors such as licking offset and touch offset to the GLM did not improve model fit (data not shown). In order to capture a physiologically realistic range of response delays to behavioral events as previously observed (Chen et al., 2013b; Chen et al., 2015), regressors for each behavioral parameter were generated across a range of delays from $i = -3$ ($t = 0.43$ s before behavior event) to $i = +6$ ($t = 0.85$ s after behavioral event). Only delays from $i = -2$ to $i = +5$ were included for cell type analysis. GLM was applied to active neurons, where the first 5 seconds from each trial across active sessions were extracted and concatenated for analysis.

To fit the GLM, trials were randomly divided into a training set (80% of trials) and a test set (20% of trials). Ridge regression was used to minimize the B_i at irrelevant delays. The optimum regularization parameter was determined by performing a 5-fold cross validation within the training set and selecting the value with the best cross validation performance. B_i was then calculated from the training set and applied to the test set to obtain predictions for Y_t . To assess GLM fit, a coefficient of determination (R^2) was calculated by comparing the predicted and the original traces. To reduce the effect of the particular choice of test trials on R^2 , test trials were bootstrapped 1000 times to obtain a final R^2 reflecting GLM fit. To assess the significance of individual B_i , a shuffled distribution for each B_i was obtained by permutation test after shuffling

calcium traces for time points within each trial 1000 times. B_i whose value was greater than the 95 percentile of the shuffled distribution was identified as significant. GLM does not require normal distribution of the data set. Comparisons of B_i across cell types was performed using one-way repeated measures ANOVA. The variances of each the cell type were tested using the F-test and determined to not be significantly different.

Trial type analysis. The performance of neuronal populations or single neurons in discriminating two trial types was assessed using a receiver operating characteristic (ROC) analysis (Green and Swets, 1966; O'Connor et al., 2010). For neuronal populations, the discriminability of the population response projected along the LD axis was measured at each time point 1 s prior to and following touch. Each trial was assigned a “discrimination variable” score (DV) equal to the similarity to the mean projected population response for trial type X minus the similarity to the mean projected population response for trial type Y . Thus, for trial type X

$$DV_x = X_i(\bar{X}_{\forall j \neq i} - \bar{Y}) \quad (11)$$

and for trial type Y

$$DV_Y = Y_i(\bar{X} - \bar{Y}_{\forall j \neq i}) \quad (12)$$

where X_i and Y_i are the single-trial population response for the i -th trial. \bar{X} and \bar{Y} are the mean population response. Trials were classified as belonging to trial type X or Y if DV_X or DV_Y was greater than a given criterion, respectively. To determine the fraction of trials an ideal observer could correctly classify, an ROC curve was constructed by varying this criterion value across the entire range of DV_X or DV_Y . At each criterion value, the probability that a trial of type X exceeded the criterion value was plotted against the probability that a trial of type Y exceeded the

criterion value. The area under the ROC curve ($A_{observed}$) was then calculated to represent the single-neuron performance (“fraction correct”) as the fraction of trials correctly discriminated by an ideal observer using the DV . We corrected for sampling bias due to the limited number of trials collected, using methods described (Safaai et al., 2013). The sampling bias (A_{bias}) was determined by calculating the mean area under the ROC curve after randomly shuffling trial type or stimulus labels repeated 1000 times. The corrected area under the ROC curve $A_{corrected}$ was then calculated as $A_{corrected} = A_{observed} - A_{bias} + 0.5$.

For single neurons, classification of trial type X versus trial type Y was based on the similarity of the calcium transient in each trial to the mean calcium transient for trial type X compared to trial type Y . Only the first second of the calcium signals following initial texture contact was considered since it reflected the minimum touch duration common across trial types (Chen et al., 2013b; Chen et al., 2015). DV was equal to the dot-product similarity to the mean calcium transient for trial type X minus the dot-product similarity to the mean for trial type Y . Neurons discriminating above chance were identified using repeated permutations tests where trial type or stimulus labels were randomly shuffled. For each permutation test, a threshold corresponding to the shuffled distribution 95th percentile was calculated. Neurons, whose performance values were above the mean value of this threshold across 1000 permutation tests, were considered to be discriminating above chance. Comparison of discriminative neurons across cell types was performed using a χ^2 test. Normal distribution was assumed for statistical comparison but not explicitly tested.

Linear discriminant analysis. We used linear discriminant analysis (LDA) for dimensionality reduction of neuronal population responses. Observations consisted of the $\Delta R/R$ values at a given

time point for all neurons simultaneously recorded within an imaging field, thus representing the neuronal state space vector at this moment (with each neuron representing one dimension), i.e., representing a ‘snapshot’ of the state space vector trajectory during the given trial. Observations were considered for all n trials, separated into the N_1 and N_2 trials for the two chosen trial conditions C_1 and C_2 , respectively (e.g., Hit vs. CR or low- vs. high-amplitude whisking; see **Table 1**). $\Delta R/R$ values were arranged in a matrix \mathbf{x} with neurons as columns and trials as rows. The LDA procedure seeks to find a projection vector w such that the projections of the observations onto this axis, collected in the vector

$$y = w^T \mathbf{x} + w_0, \quad (13)$$

are best separated for the two chosen trial conditions. Maximal separation is defined as the maximal difference of the mean vectors $\mu_1 = \frac{1}{N_1} \sum_{n \in C_1} x_n$ and $\mu_2 = \frac{1}{N_2} \sum_{n \in C_2} x_n$ for C_1 and C_2 , respectively, normalized by the within-class scatter. The solution, known as Fisher’s linear discriminant (Fisher, 1936; Safaai et al., 2013), is given by

$$w^T = S_w^{-1}(\mu_1 - \mu_2) \quad (14)$$

where S_w^{-1} is the within-class covariance given by

$$S_w^{-1} = \sum_{n \in C_1} (x_n - \mu_1)(x_n - \mu_1)^T + \sum_{n \in C_2} (x_n - \mu_2)(x_n - \mu_2)^T \quad (15)$$

The bias is calculated as

$$w_0 = -\frac{1}{2}(w^T \mu_1 - w^T \mu_2) \quad (16)$$

Intuitively, this procedure finds the hyperplane in the state space (orthonormal to the projection vector w and encompassing w_0) that results in best separation according to Fisher’s criterion.

To analyze the time courses of neuronal population dynamics during behavior trials, the LDA procedure was applied independently to each time point over 1-s periods before and after whisker-touch onset (or licking onset in some cases). Only neurons identified as active in at least

one imaging session were included in the LDA. For each individual trial we thereby obtained a time-dependent ‘linear discriminant’ variable $LD(t)$. The mean value \overline{LD} by definition is half of the distance between the projections of the mean vectors μ_1 and μ_2

$$\overline{LD}(t) = \frac{1}{2}(w^T \mu_1 + w^T \mu_2) \quad (17)$$

For whole-region analysis (S1 or S2) we averaged LD values obtained from all imaging areas/planes.

Inter-areal coordination as a function of time, termed $LDCC_{S1:S2}$, was determined by calculating the Pearson’s correlation coefficient between the population responses LD_{S1} and LD_{S2} for S1 and S2, respectively, across all simultaneously imaged trials at each time point. To determine the specific contribution of $S1_{S2}$ or $S2_{S1}$ neurons to cross-areal coordination, a one-dimensional modified discriminant $LD'(t)$ was obtained for each area by shuffling the trial-by-trial calcium responses of $S1_{S2}$ or $S2_{S1}$ neurons, respectively, and then projecting the population vector onto the LDA axis determined from the non-shuffled population response. Cross-correlation of LD'_{S1} and LD'_{S2} yielded $LDCC'_{S1:S2}$. Shuffling was repeated 1000 times to obtain mean and standard error for $LDCC'_{S1:S2}$ values. The change in S1-S2 correlation ($\Delta LDCC_{S1:S2}$) was calculated as the mean $LDCC'_{S1:S2}$ minus the unshuffled $LDCC_{S1:S2}$. Reductions in correlation strength thus show up as negative values. To control for trial shuffling of $S1_{S2}$ or $S2_{S1}$ neurons, trial shuffling was performed on an equal number of $S1_{ND}$ or $S2_{ND}$ neurons, repeated 1000 times, and $\Delta LDCC_{S1:S2}$ was calculated from the average cross-correlation.

Comparisons of $LDCC_{S1:S2}$ and $\Delta LDCC_{S1:S2}$ across trial conditions were performed using one-way repeated measures ANOVA. The variances of each the trial condition were tested using the F-test and determined to not be significantly different.

References

- Akemann, W., Sasaki, M., Mutoh, H., Imamura, T., Honkura, N., and Knöpfel, T. (2013). Two-photon voltage imaging using a genetically encoded voltage indicator. *Sci Rep* 3, 2231.
- Akerboom, J., Carreras Calderon, N., Tian, L., Wabnig, S., Prigge, M., Tolo, J., Gordus, A., Orger, M.B., Severi, K.E., Macklin, J.J., *et al.* (2013). Genetically encoded calcium indicators for multi-color neural activity imaging and combination with optogenetics. *Front Mol Neurosci* 6, 2.
- Aronoff, R., Matyas, F., Mateo, C., Ciron, C., Schneider, B., and Petersen, C.C. (2010). Long-range connectivity of mouse primary somatosensory barrel cortex. *Eur J Neurosci* 31, 2221-2233.
- Bathellier, B., Ushakova, L., and Rumpel, S. (2012). Discrete neocortical dynamics predict behavioral categorization of sounds. *Neuron* 76, 435-449.
- Bosman, L.W., Houweling, A.R., Owens, C.B., Tanke, N., Shevchouk, O.T., Rahmati, N., Teunissen, W.H., Ju, C., Gong, W., Koekkoek, S.K., *et al.* (2011). Anatomical pathways involved in generating and sensing rhythmic whisker movements. *Front Integr Neurosci* 5, 53.
- Brecht, M., Schneider, M., Sakmann, B., and Margrie, T.W. (2004). Whisker movements evoked by stimulation of single pyramidal cells in rat motor cortex. *Nature* 427, 704-710.
- Bressler, S.L., and Menon, V. (2010). Large-scale brain networks in cognition: emerging methods and principles. *Trends Cogn Sci* 14, 277-290.
- Buschman, T.J., and Miller, E.K. (2007). Top-down versus bottom-up control of attention in the prefrontal and posterior parietal cortices. *Science* 315, 1860-1862.
- Cai, D., Cohen, K.B., Luo, T., Lichtman, J.W., and Sanes, J.R. (2013). Improved tools for the Brainbow toolbox. *Nature Methods* 10, 540-547.
- Chen, J.L., Andermann, M.L., Keck, T., Xu, N.L., and Ziv, Y. (2013a). Imaging neuronal populations in behaving rodents: paradigms for studying neural circuits underlying behavior in the mammalian cortex. *J Neurosci* 33, 17631-17640.
- Chen, J.L., Carta, S., Soldado-Magraner, J., Schneider, B.L., and Helmchen, F. (2013b). Behaviour-dependent recruitment of long-range projection neurons in somatosensory cortex. *Nature* 499, 336-340.
- Chen, J.L., Margolis, D.J., Stankov, A., Sumanovski, L.T., Schneider, B.L., and Helmchen, F. (2015). Pathway-specific reorganization of projection neurons in somatosensory cortex during learning. *Nature Neurosci* 18, 1101-1108.
- Cheng, A., Goncalves, J.T., Golshani, P., Arisaka, K., and Portera-Cailliau, C. (2011). Simultaneous two-photon calcium imaging at different depths with spatiotemporal multiplexing. *Nature Methods* 8, 139-142.
- Cong, F., Lin, Q.H., Kuang, L.D., Gong, X.F., Astikainen, P., and Ristaniemi, T. (2015). Tensor decomposition of EEG signals: a brief review. *J Neurosci Meth* 248, 59-69.
- Deschenes, M., Veinante, P., and Zhang, Z.W. (1998). The organization of corticothalamic projections: reciprocity versus parity. *Brain research Brain Research Reviews* 28, 286-308.
- Diamond, M.E., von Heimendahl, M., Knutsen, P.M., Kleinfeld, D., and Ahissar, E. (2008). 'Where' and 'what' in the whisker sensorimotor system. *Nat Rev Neurosci* 9, 601-612.

1124 Fenno, L.E., Mattis, J., Ramakrishnan, C., Hyun, M., Lee, S.Y., He, M., Tucciarone, J., Selimbeyoglu, A., Berndt,
1125 A., Grosenick, L., *et al.* (2014). Targeting cells with single vectors using multiple-feature Boolean logic. *Nature*
1126 *Methods* *11*, 763-772.

1127 Ferezou, I., Haiss, F., Gentet, L.J., Aronoff, R., Weber, B., and Petersen, C.C. (2007). Spatiotemporal dynamics of
1128 cortical sensorimotor integration in behaving mice. *Neuron* *56*, 907-923.

1129 Fisher, R. (1936). The use of multiple measurements in taxonomic problems. *Annals Eugen* *7*, 179-188.

1130 Gilbert, C.D., and Li, W. (2013). Top-down influences on visual processing. *Nature Rev Neurosci* *14*, 350-363.

1131 Glickfeld, L.L., Andermann, M.L., Bonin, V., and Reid, R.C. (2013). Cortico-cortical projections in mouse visual
1132 cortex are functionally target specific. *Nature Neurosci* *16*, 219-226.

1133 Green, D.M., and Swets, J.A. (1966). *Signal detection theory and psychophysics* (Wiley).

1134 Grewe, B.F., Langer, D., Kasper, H., Kampa, B.M., and Helmchen, F. (2010). High-speed in vivo calcium imaging
1135 reveals neuronal network activity with near-millisecond precision. *Nature Methods* *7*, 399-405.

1136 Grewe, B.F., Voigt, F.F., van 't Hoff, M., and Helmchen, F. (2011). Fast two-layer two-photon imaging of neuronal
1137 cell populations using an electrically tunable lens. *Biomed Opt Express* *2*, 2035-2046.

1138 Hitchcock, F.L. (1927). The Expression of a Tensor or a Polyadic as a Sum of Products. *Journal of Mathematics and*
1139 *Physics* *6*, 164-189.

1140 Horikawa, K., Yamada, Y., Matsuda, T., Kobayashi, K., Hashimoto, M., Matsu-ura, T., Miyawaki, A., Michikawa,
1141 T., Mikoshiba, K., and Nagai, T. (2010). Spontaneous network activity visualized by ultrasensitive Ca²⁺
1142 indicators, yellow Cameleon-Nano. *Nature Methods* *7*, 729-732.

1143 Huber, D., Gutnisky, D.A., Peron, S., O'Connor, D.H., Wiegert, J.S., Tian, L., Oertner, T.G., Looger, L.L., and
1144 Svoboda, K. (2012). Multiple dynamic representations in the motor cortex during sensorimotor learning. *Nature*
1145 *484*, 473-478.

1146 Hutchison, R.M., Womelsdorf, T., Allen, E.A., Bandettini, P.A., Calhoun, V.D., Corbetta, M., Della Penna, S., Duyn,
1147 J.H., Glover, G.H., Gonzalez-Castillo, J., *et al.* (2013). Dynamic functional connectivity: promise, issues, and
1148 interpretations. *Neuroimage* *80*, 360-378.

1149 Jarosiewicz, B., Schummers, J., Malik, W.Q., Brown, E.N., and Sur, M. (2012). Functional biases in visual cortex
1150 neurons with identified projections to higher cortical targets. *Current Biology* *22*, 269-277.

1151 Kleinfeld, D., and Deschenes, M. (2011). Neuronal basis for object location in the vibrissa scanning sensorimotor
1152 system. *Neuron* *72*, 455-468.

1153 Knutsen, P.M., Derdikman, D., and Ahissar, E. (2005). Tracking whisker and head movements in unrestrained
1154 behaving rodents. *J Neurophysiol* *93*, 2294-2301.

1155 Komiyama, T., Sato, T.R., O'Connor, D.H., Zhang, Y.X., Huber, D., Hooks, B.M., Gabbito, M., and Svoboda, K.
1156 (2010). Learning-related fine-scale specificity imaged in motor cortex circuits of behaving mice. *Nature* *464*,
1157 1182-1186.

1158 Lecoq, J., Savall, J., Vucinic, D., Grewe, B.F., Kim, H., Li, J.Z., Kitch, L.J., and Schnitzer, M.J. (2014). Visualizing
1159 mammalian brain area interactions by dual-axis two-photon calcium imaging. *Nature Neurosci* *17*, 1825-1829.

1160 Lim, D.H., Ledue, J., Mohajerani, M.H., Vanni, M.P., and Murphy, T.H. (2013). Optogenetic approaches for
1161 functional mouse brain mapping. *Frontiers in Neuroscience* *7*, 54.

1162 Lütcke, H., Gerhard, F., Zenke, F., Gerstner, W., and Helmchen, F. (2013). Inference of neuronal network spike
 1163 dynamics and topology from calcium imaging data. *Front Neural Circuits* 7, 201.
 1164 Madisen, L., Garner, A.R., Shimaoka, D., Chuong, A.S., Klapoetke, N.C., Li, L., van der Bourg, A., Niino, Y., Eglf,
 1165 L., Monetti, C., *et al.* (2015). Transgenic mice for intersectional targeting of neural sensors and effectors with
 1166 high specificity and performance. *Neuron* 85, 942-958.
 1167 Markov, N.T., Ercsey-Ravasz, M., Van Essen, D.C., Knoblauch, K., Toroczkai, Z., and Kennedy, H. (2013). Cortical
 1168 high-density counterstream architectures. *Science* 342, 1238406.
 1169 Matsuda, T., and Cepko, C.L. (2007). Controlled expression of transgenes introduced by in vivo electroporation.
 1170 *Proceedings of the National Academy of Sciences of the United States of America* 104, 1027-1032.
 1171 Melzer, P., Champney, G.C., Maguire, M.J., and Ebner, F.F. (2006). Rate code and temporal code for frequency of
 1172 whisker stimulation in rat primary and secondary somatic sensory cortex. *Exp Brain Res* 172, 370-386.
 1173 Minderer, M., Liu, W., Sumanovski, L.T., Kügler, S., Helmchen, F., and Margolis, D.J. (2012). Chronic imaging of
 1174 cortical sensory map dynamics using a genetically encoded calcium indicator. *J Physiol* 590, 99-107.
 1175 Miri, A., Daie, K., Burdine, R.D., Aksay, E., and Tank, D.W. (2011). Regression-based identification of behavior-
 1176 encoding neurons during large-scale optical imaging of neural activity at cellular resolution. *J Neurophysiol* 105,
 1177 964-980.
 1178 Moore, J.D., Mercer Lindsay, N., Deschenes, M., and Kleinfeld, D. (2015). Vibrissa Self-Motion and Touch Are
 1179 Reliably Encoded along the Same Somatosensory Pathway from Brainstem through Thalamus. *PLoS Biol* 13,
 1180 e1002253.
 1181 Musall, S., von der Behrens, W., Mayrhofer, J.M., Weber, B., Helmchen, F., and Haiss, F. (2014). Tactile frequency
 1182 discrimination is enhanced by circumventing neocortical adaptation. *Nature Neurosci* 17, 1567-1573.
 1183 O'Connor, D.H., Peron, S.P., Huber, D., and Svoboda, K. (2010). Neural activity in barrel cortex underlying vibrissa-
 1184 based object localization in mice. *Neuron* 67, 1048-1061.
 1185 Oh, S.W., Harris, J.A., Ng, L., Winslow, B., Cain, N., Mihalas, S., Wang, Q., Lau, C., Kuan, L., Henry, A.M., *et al.*
 1186 (2014). A mesoscale connectome of the mouse brain. *Nature* 508:207-214
 1187 Pais-Vieira, M., Lebedev, M.A., Wiest, M.C., and Nicolelis, M.A. (2013). Simultaneous top-down modulation of the
 1188 primary somatosensory cortex and thalamic nuclei during active tactile discrimination. *J Neurosci* 33, 4076-4093.
 1189 Petreanu, L., Gutnisky, D.A., Huber, D., Xu, N.L., O'Connor, D.H., Tian, L., Looger, L., and Svoboda, K. (2012).
 1190 Activity in motor-sensory projections reveals distributed coding in somatosensation. *Nature* 489, 299-303.
 1191 Piatkevich, K.D., Hult, J., Subach, O.M., Wu, B., Abdulla, A., Segall, J.E., and Verkhusha, V.V. (2010). Monomeric
 1192 red fluorescent proteins with a large Stokes shift. *Proc. Natl. Acad. Sci. USA* 107, 5369-5374.
 1193 Pierret, T., Lavalley, P., and Deschenes, M. (2000). Parallel streams for the relay of vibrissal information through
 1194 thalamic barreloids. *J Neurosci* 20, 7455-7462.
 1195 Pinto, L., and Dan, Y. (2015). Cell-Type-Specific Activity in Prefrontal Cortex during Goal-Directed Behavior.
 1196 *Neuron* 87, 437-450.
 1197 Quirin, S., Jackson, J., Peterka, D.S., and Yuste, R. (2014). Simultaneous imaging of neural activity in three
 1198 dimensions. *Front Neural Circuits* 8, 29.

- Saalmann, Y.B., Pinsk, M.A., Wang, L., Li, X., and Kastner, S. (2012). The pulvinar regulates information transmission between cortical areas based on attention demands. *Science* 337, 753-756.
- Safaai, H., von Heimendahl, M., Sorando, J.M., Diamond, M.E., and Maravall, M. (2013). Coordinated population activity underlying texture discrimination in rat barrel cortex. *J Neurosci* 33, 5843-5855.
- Salinas, E., and Sejnowski, T.J. (2001). Correlated neuronal activity and the flow of neural information. *Nature Rev Neurosci* 2, 539-550.
- Sato, T.R., and Svoboda, K. (2010). The functional properties of barrel cortex neurons projecting to the primary motor cortex. *J Neurosci* 30, 4256-4260.
- Seely, J.S., Cunningham, J.P., Lara, H., and Churchland, M.M. (2014). Should one collect more trials, more neurons, or more conditions: a statistical solution to the experimentalist's dilemma. *Society for Neuroscience Abstracts*, 188.125/UU185.
- Sherman, S.M., and Guillery, R.W. (2011). Distinct functions for direct and transthalamic corticocortical connections. *Journal of Neurophysiology* 106, 1068-1077.
- Stirman, J.N., Smith, I.T., Kudenov, M.W., and Smith, S.L. (2014). Wide field-of-view, twin-region two-photon imaging across extended cortical networks. *bioRxiv*. doi: <http://dx.doi.org/10.1101/011320>
- Sun, X.R., Badura, A., Pacheco, D.A., Lynch, L.A., Schneider, E.R., Taylor, M.P., Hogue, I.B., Enquist, L.W., Murthy, M., and Wang, S.S. (2013). Fast GCaMPs for improved tracking of neuronal activity. *Nat Commun* 4, 2170.
- Suter, B.A., and Shepherd, G.M. (2015). Reciprocal interareal connections to corticospinal neurons in mouse M1 and S2. *J Neurosci* 35, 2959-2974.
- Theyel, B.B., Llano, D.A., and Sherman, S.M. (2010). The corticothalamocortical circuit drives higher-order cortex in the mouse. *Nat Neurosci* 13, 84-88.
- Tsai, P.S., Mateo, C., Field, J.J., Schaffer, C.B., Anderson, M.E., and Kleinfeld, D. (2015). Ultra-large field-of-view two-photon microscopy. *Opt Express* 23, 13833-13847.
- Yamashita, T., Pala, A., Pedrido, L., Kremer, Y., Welker, E., and Petersen, C.C. (2013). Membrane potential dynamics of neocortical projection neurons driving target-specific signals. *Neuron* 80, 1477-1490.
- Yang, H., Kwon, S.E., Severson, K.S., and O'Connor, D.H. (2016). Origins of choice-related activity in mouse somatosensory cortex. *Nat Neurosci* 19, 127-134.
- Yu, C., Derdikman, D., Haidarliu, S., and Ahissar, E. (2006). Parallel thalamic pathways for whisking and touch signals in the rat. *PLoS biology* 4, e124.
- Zagha, E., Casale, A.E., Sachdev, R.N., McGinley, M.J., and McCormick, D.A. (2013). Motor cortex feedback influences sensory processing by modulating network state. *Neuron* 79, 567-578.
- Zingg, B., Hintiryan, H., Gou, L., Song, M.Y., Bay, M., Bienkowski, M.S., Foster, N.N., Yamashita, S., Bowman, I., Toga, A.W., *et al.* (2014). Neural networks of the mouse neocortex. *Cell* 156, 1096-1111.

Figure 1

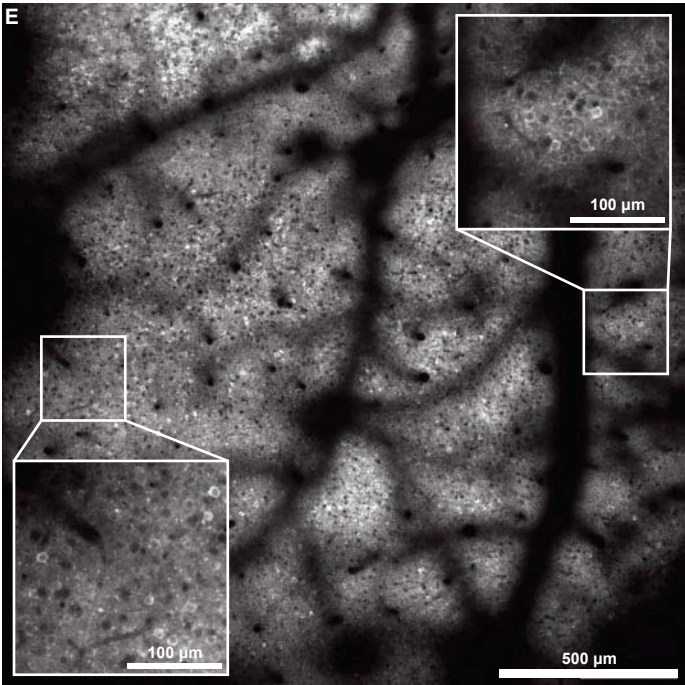
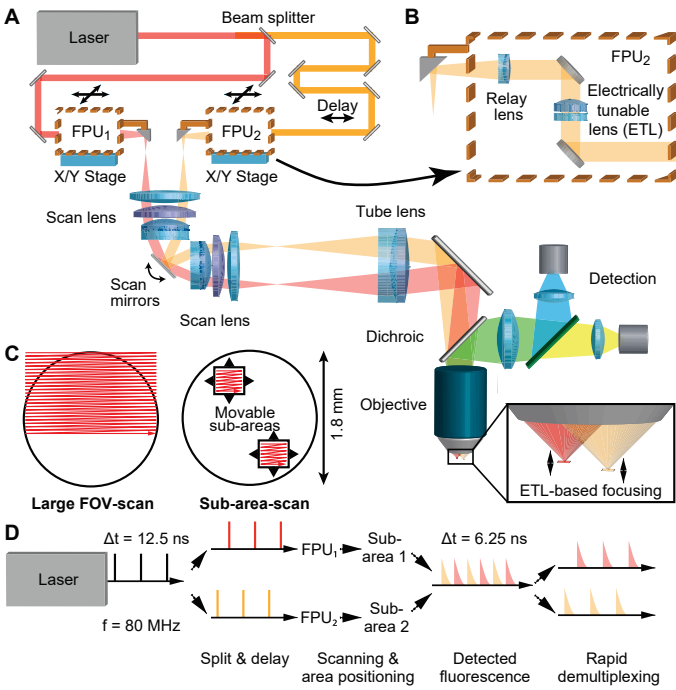


Figure 2

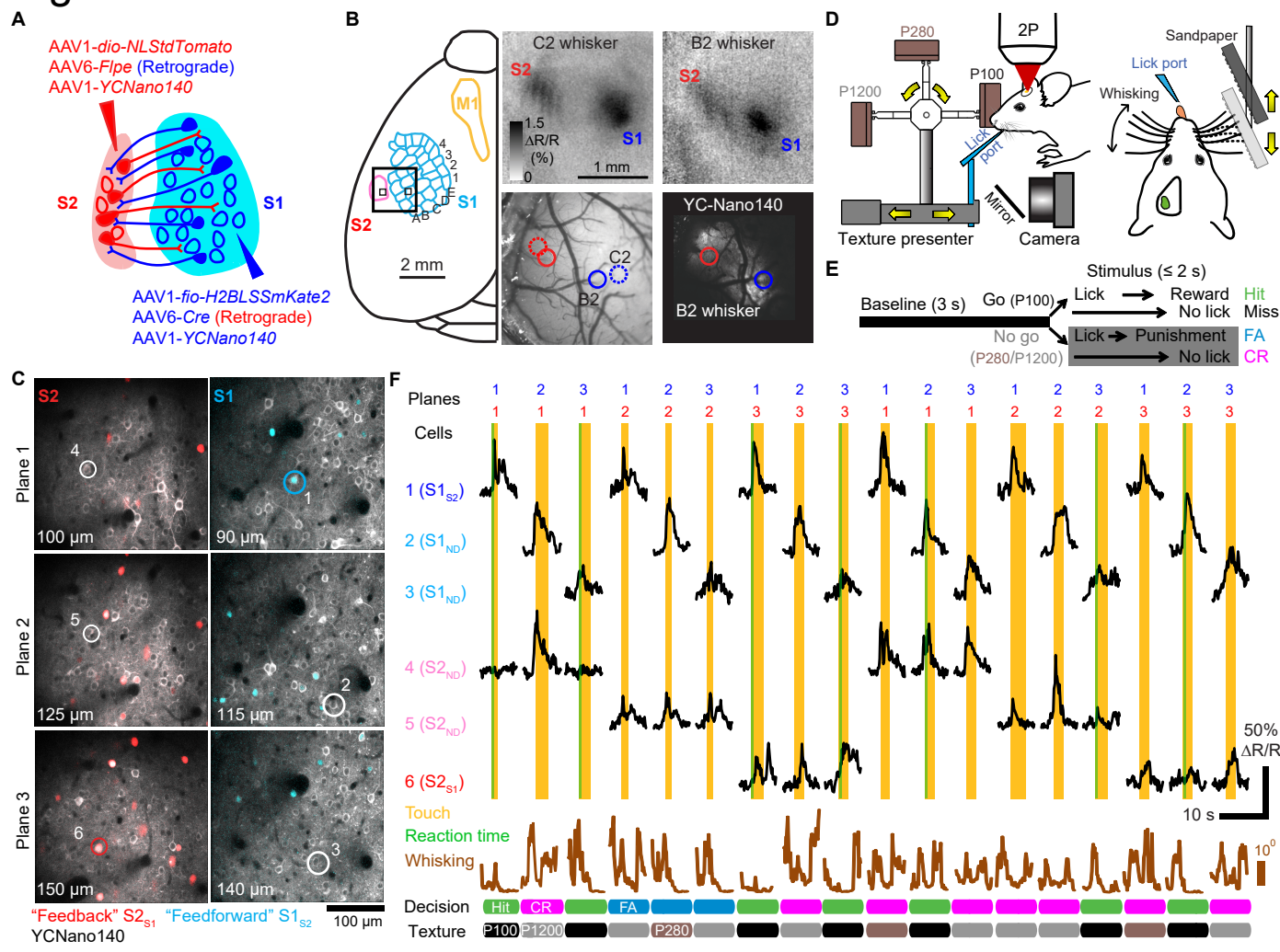


Figure 3

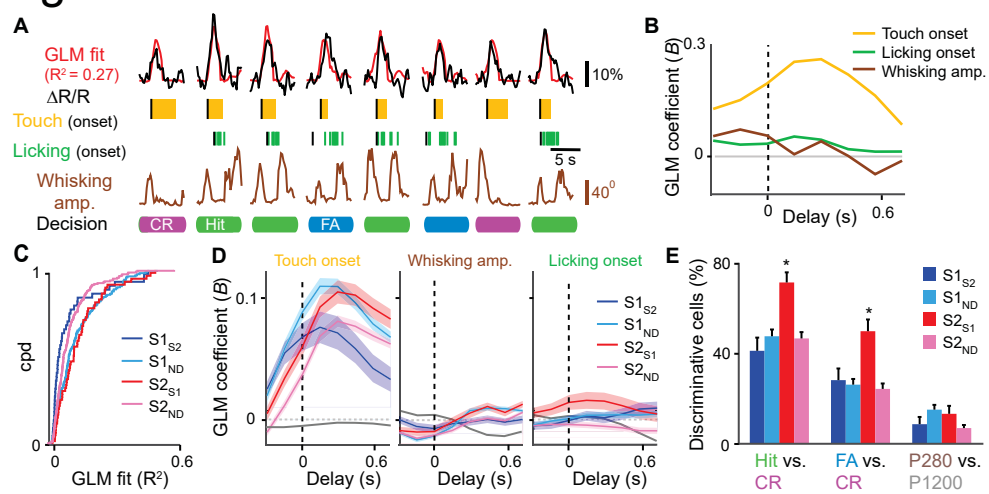


Figure 4

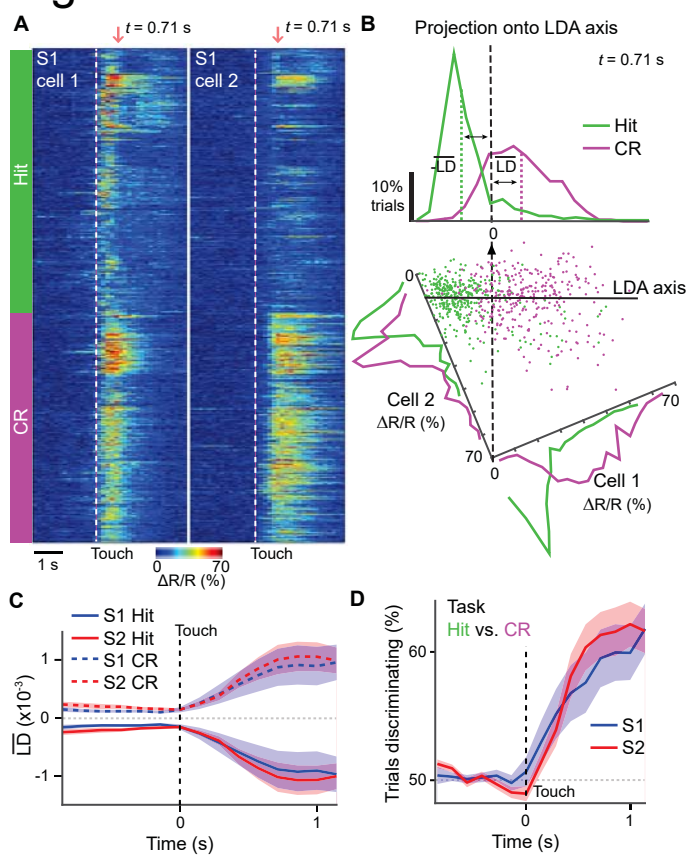


Figure 5

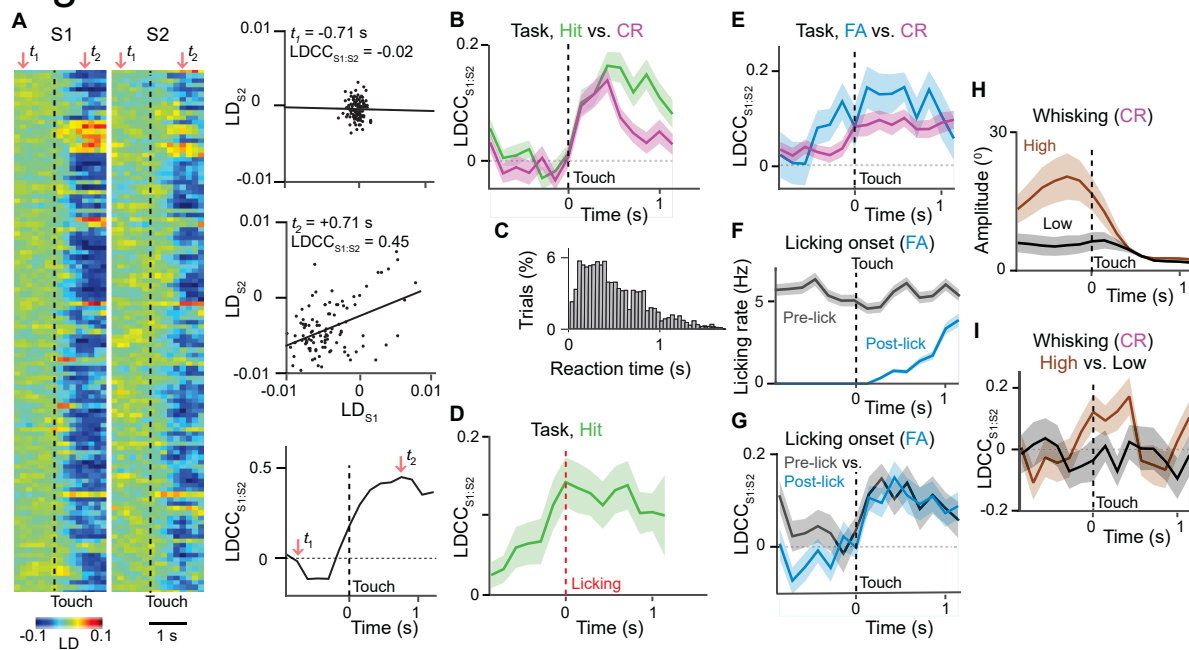


Figure 6

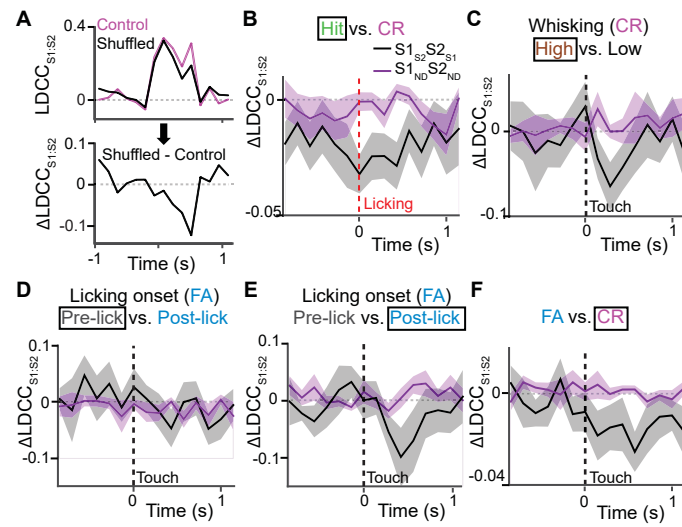


Figure 7

